Systems/Circuits

Inhibition in Simple Cell Receptive Fields Is Broad and OFF-Subregion Biased

M. Morgan Taylor, Madineh Sedigh-Sarvestani, Leif Vigeland, Larry A. Palmer, and Diego Contreras
Mahoney Institute for Neurosciences, Perelman School of Medicine, University of Pennsylvania, Philadelphia, Pennsylvania 19104

Inhibition in thalamorecipient layer 4 simple cells of primary visual cortex is believed to play important roles in establishing visual response properties and integrating visual inputs across their receptive fields (RFs). Simple cell RFs are characterized by nonoverlapping, spatially restricted subregions in which visual stimuli can either increase or decrease the firing rate of the cell, depending on contrast. Inhibition is believed to be triggered exclusively from visual stimulation of individual RF subregions. However, this view is at odds with the known anatomy of layer 4 interneurons in visual cortex and differs from recent findings in mouse visual cortex. Here we show with *in vivo* intracellular recordings in cats that while excitation is restricted to RF subregions, inhibition spans the width of simple cell RFs. Consequently, excitatory stimuli within a subregion concomitantly drive excitation and inhibition. Furthermore, we found that the distribution of inhibition across the RF is stronger toward OFF subregions. This inhibitory OFF-subregion bias has a functional consequence on spatial integration of inputs across the RF. A model based on the known anatomy of layer 4 demonstrates that the known proportion and connectivity of inhibitory neurons in layer 4 of primary visual cortex is sufficient to explain broad inhibition with an OFF-subregion bias while generating a variety of phase relations, including antiphase, between excitation and inhibition in response to drifting gratings.

Key words: **conductances; inhibitory interneuron; input integration; intracellular recordings; primary visual cortex; push–pull**

Significance Statement

The wiring of excitatory and inhibitory neurons in cortical circuits is key to determining the response properties in sensory cortex. In the visual cortex, the first cells that receive visual input are simple cells in layer 4. The underlying circuitry responsible for the response properties of simple cells is not yet known. In this study, we challenge a long-held view concerning the pattern of inhibitory input and provide results that agree with current known anatomy. We show here that inhibition is evoked broadly across the receptive fields of simple cells, and we identify a surprising bias in inhibition within the receptive field. Our findings represent a step toward a unified view of inhibition across different species and sensory systems.

Introduction

In primary visual cortex (V1), the receptive fields (RFs) of thalamorecipient layer 4 (L4) neurons called simple cells are characterized by elongated, nonoverlapping subregions (Hubel and Wiesel, 1962). In each subregion, increases (ON subregions) or decreases (OFF subregions) in light level cause an increase in the firing rate of the cell, while the opposite light change decreases the firing rate. This property is known as the push–pull organization of the RF (Palmer and Davis, 1981; Ferster, 1988). Intracellular studies in simple cells showed that the push–pull pattern of firing rate corresponds with depolarization (push) and hyperpolarization (pull) of the membrane potential (Ferster, 1986; Hirsch et al., 1998; Fig. 1*A*, scheme).

The push–pull behavior of spike output and membrane potential is currently believed to rely on excitatory glutamatergic and inhibitory GABAergic synaptic inputs restricted spatially to RF subregions (Ferster, 1988; Hirsch et al., 1998; Troyer et al., 1998; Anderson et al., 2000; Ferster and Miller, 2000; Miller et al., 2001; Hirsch, 2003; Alitto and Dan, 2010; Fig. 1*B*, scheme). Support for this model comes from intracellular estimates of synaptic conductances in response to drifting gratings or moving bars, revealing their modulation in apparent temporal antiphase such that maximal excitation often coincided with minimal inhibition, although a variety of phase relations was also observed (Ferster, 1988; Anderson et al., 2000; Monier et al., 2003, 2008; Tan et al., 2011). This suggested a simple underlying functional connectivity

Received July 25, 2017; revised Sept. 11, 2017; accepted Oct. 2, 2017.

Author contributions: M.M.T., L.V., L.A.P., and D.C. designed research; M.M.T., M.S.-S., L.V., L.A.P., and D.C. performed research; M.M.T. contributed unpublished reagents/analytic tools; M.M.T. and M.S.-S. analyzed data; M.M.T. and D.C. wrote the paper.

This work was supported by National Institutes of Health Grant R01EY027205 (D.C.), National Science Foundation Grant GRFP DGE-1321851 (M.M.T.), and the University of Pennsylvania Vision Training Grant T32 EY007035-38 (M.M.T., D.C.). We thank J.A. Cardin for assistance with data collection, and the anonymous reviewer for insightful comments on the manuscript.

The authors declare no competing financial interests.

Correspondence should be addressed to Diego Contreras, Mahoney Institute for Neurosciences, Perelman School of Medicine, University of Pennsylvania, Philadelphia, PA 19104. E-mail: diegoc@upenn.edu.

DOI:10.1523/JNEUROSCI.2099-17.2017

 0270-6474/18/380595-18$15.00/0

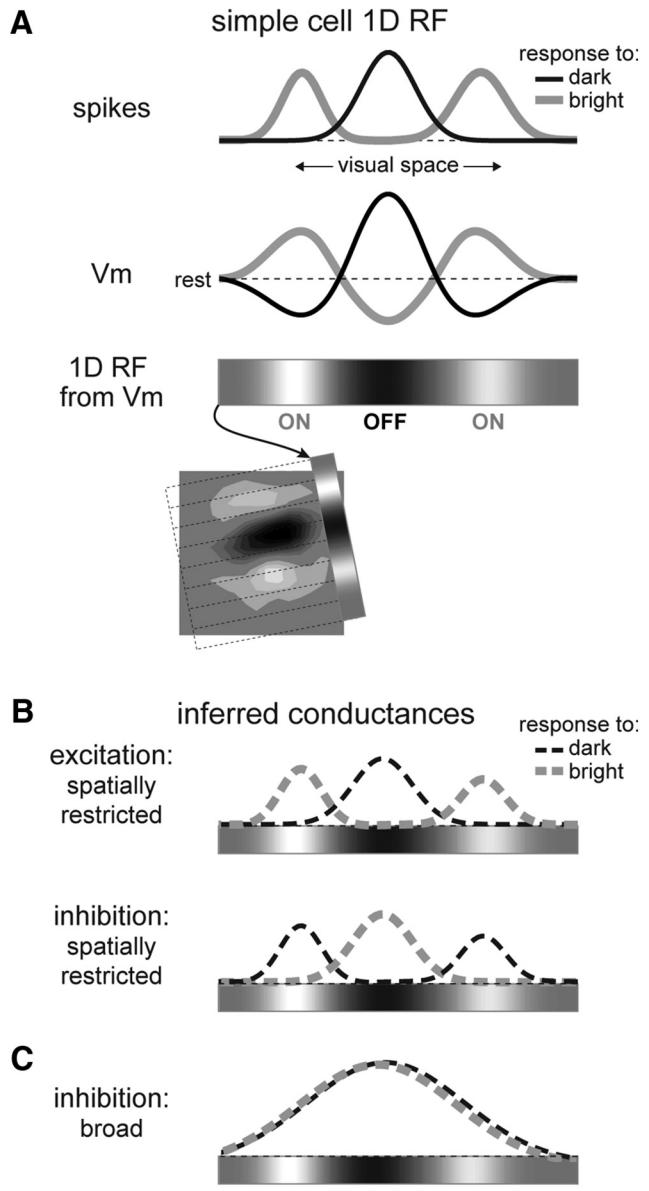

Figure 1. Push–pull organization of simple cell receptive fields. ***A***, Top, Schematized spike and V_m responses characterizing the 1D RF of a simple cell. Bottom, Grayscale colorbar representation of the 1D RF, calculated from Gaussian fits to V_m depolarizing responses to bright minus dark. Inset shows agreement between 1D and 2D RF estimates for an example cell (data shown in Fig. 2). ***B***, Possible arrangements of synaptic conductances proposed to underlie the V_m responses. Classically, excitatory (top) and inhibitory (bottom) inputs are assumed to be arranged in a spatially restricted and antiphase organization, matching the patterns of V_m depolarization and hyperpolarization, respectively. ***C***, We test the hypothesis that inhibition is broad across the RF.

between inhibitory and excitatory simple cells with iso-oriented but spatially antiphase RFs (Ferster, 1988; Hirsch et al., 1998; Troyer et al., 1998; Anderson et al., 2000). The assumption of spatially restricted inhibitory connectivity in V1 L4 remains dominant and is used in computer models of the V1 circuit (Azzopardi et al., 2014; Kremkow et al., 2016b).

Yet, as shown in other sensory systems (Wehr and Zador, 2003; Wilent and Contreras, 2005; Higley and Contreras, 2006; Heiss et al., 2008; Poo and Isaacson, 2009; Isaacson and Scanziani, 2011; Cossell et al., 2015; Frégnac and Bathellier, 2015) and also during spontaneous brain activity (Haider et al., 2006; Rudolph et al., 2007), the trajectory of the membrane potential is always determined by a balance between excitation and inhibition. Given the ubiquitous nature of inhibition in the brain, concomitant excitation and inhibition is more likely than spatially restricted inhibition.

Furthermore, while a precise spatial arrangement of excitation is compatible with the precise alignment of the thalamocortical excitatory input to L4 simple cells (Reid and Alonso, 1995; Alonso et al., 2001; Sedigh-Sarvestani et al., 2017), a similar spatial arrangement of inhibitory synaptic input is difficult to reconcile with the small proportion of inhibitory neurons in L4 (Gabbott and Somogyi, 1986) and their dense axonal arborizations and apparently indiscriminate connectivity (Ramón y Cajal, 1909; Kisvárday et al., 1985; Ahmed et al., 1997; Binzegger et al., 2004). Particularly, given the variability of simple cell RF shapes and spatial phases (Jones and Palmer, 1987a; Wang et al., 2015), spatially restricted inhibition would require at least equal numbers of inhibitory and excitatory neurons.

Here we show in cat V1 *in vivo* that, unlike excitation, inhibition is spatially widespread across the width of the RF of L4 simple cells (Fig. 1*C*, scheme). Therefore, as expected from the anatomy and from results in other primary sensory areas, excitatory visual stimuli within individual RF subregions evoke concomitant excitation and inhibition. We also show that inhibition is surprisingly biased toward OFF subregions, in agreement with recent findings that simple cell RFs are anchored by OFF inputs (Jin et al., 2011; Kremkow et al., 2016a; Lee et al., 2016b). A simple model demonstrates that indiscriminate inhibitory connectivity generates broad inhibition and can produce modulated excitation and inhibition with a variety of spatial phase offsets in response to drifting gratings.

Materials and Methods

Subjects. Experiments were performed on 33 adult male cats (2.5–3.5 kg). All experiments were conducted in accordance with the ethical guidelines of the National Institutes of Health and with the approval of the Institutional Animal Care and Use Committee at the University of Pennsylvania.

Surgical protocol. Surgical methods were as previously reported (Cardin et al., 2010; Vigeland et al., 2013). Animals were anesthetized with an initial intraperitoneal injection of thiopental (25 mg/kg) or Nembutal (25 mg/kg) and supplemental isoflurane (2–4% in a 70:30 mixture of N_2O and O_2). Subsequently, the animal was paralyzed with gallamine triethiodide (Flaxedil) and artificially ventilated, keeping the end-tidal CO_2 concentration at 3.9 ± 0.2%. Anesthesia was maintained with a continuous intravenous infusion of thiopental (3–10 mg/kg/h) for the duration of the experiment (14–16 h). Heart rate, blood pressure, and EEG were monitored throughout the experiment, and the rectal temperature was maintained at 37–38°C with a heating pad.

To expose visual cortex, a craniotomy centered at Horsley-Clarke coordinates posterior 4.0 and lateral 2.0 was performed, and the underlying dura was removed. The stability of recordings was improved by a bilateral pneumothorax, drainage of the cisterna magna, and hip suspension, and by injecting a warm solution of agar (3.5–4%) between the dura and the brain.

Intracellular recordings. The results described here are based on intracellular recordings from 41 simple cells in area 17. Sharp electrode recordings were performed with glass micropipettes (50–80 MΩ) filled with 3 M potassium acetate (KAc). Access resistance of each pipette was compensated on-line (bridge balancing). In a subset of experiments (n = 12 cells), we included lidocaine *N*-ethyl bromide (QX-314; 100 mM) in the recording pipette to block voltage-gated sodium channels (Connors and Prince, 1982) and voltage-gated potassium and calcium conductances (Mulle et al., 1985). In these cells, visual stimuli were presented at least 4 min after initial impalement to allow diffusion of the drug into the cell and effective blockade of action potentials. We did not use cesium in the pipette because this is only useful in voltage-clamp recordings in which the voltage is kept constant. In our current-clamp condition, cesium blocks leak potassium currents and prolongs synaptic responses

and the duration of action potentials by tens to hundreds of milliseconds, making the study of brief sensory responses impossible.

All cells had a stable resting membrane potential (V_m) more negative than −60 mV. The mean ± SD resting conductance was 27.3 ± 11.4 nS. Regular-spiking (RS; $n = 30$) and fast-spiking (FS; $n = 8$) cells were distinguished by their firing pattern in response to depolarizing current injection and spike waveform characteristics, as described previously by Cardin et al. (2007). For recordings with QX-314, this was based on spikes at the beginning of the recordings, before action potentials became blocked. Three fast rhythmic bursting (FRB) cells were identified based on the distribution of interspike intervals showing a characteristic peak at ~40 Hz. Laminar location was estimated from the position of the electrode, which agrees with measurements from *post hoc* morphological reconstructions (Cardin et al., 2007). All simple cells were recorded between 480 and 1980 μm from the pial surface, with 63% of cells between 600 and 900 μm, consistent with L4. The deep simple cells were likely either from L6 or from L4 of the medial bank of area 17.

To estimate synaptic conductances, visual stimuli (described below) were presented while holding the cell at one of three to seven V_m levels, with brief somatic current pulses injected through the recording pipette. The current injection started at least 40 ms before the visual stimulus to avoid capacitative artifacts. Visual stimulus conditions and V_m levels were randomly interleaved. Input resistance (R_{in}) was monitored from the most hyperpolarizing current injections, which were also used to estimate the cell capacitance. Only datasets with stable baseline V_m and R_{in} values (<20% change from initial values) throughout the duration of visual stimuli were included.

Visual stimulation. The corneas were protected with neutral contact lenses after dilating the pupil with 1% ophthalmic atropine and retraction of the nictitating membrane with 1% phenylephrine HCl (Neo-Synephrine). Spectacle lenses were chosen by the tapetal reflection technique to optimize the focus of stimuli on the retina. The position of the monitor was adjusted to center the area centralis on the screen. Stimuli were presented on an Image Systems model M09LV monochrome monitor operating at 125 frames/s, a spatial resolution of 1024 × 786, and a mean luminance of 47 cd/m^2. The screen subtends 36° × 27° (28.7 pixels/°), and lookup tables were linearized for a contrast range of ±100%. Stimuli were generated by custom software writing to the framestore portion of a Cambridge Research Systems visual stimulus generation card mounted in a conventional PC. Custom software also allowed the display of acquired signals (V_m and spikes) on-line. Computer-assisted hand-plotting routines were used with every cell to provide initial estimates of critical parameters, especially the RF location and orientation of the cell and spatial frequency preferences. Final analysis was performed off-line from records stored on a Nicolet Vision portable data recorder (Thermo Fisher Scientific), which included V_m, injected current (I_{inj}), and stimulus marks, all sampled at 10 kHz and 16 bits.

To map two-dimensional (2D) receptive fields, precomputed frames of low-pass filtered ternary 2D dense noise were presented as 16 × 16 squares in space covering 2° × 2° to 4° × 4°, with a frame duration of 16 ms. For 1D analysis, we used flashed bright and dark bars ($n = 8$–16; duration 40–160 ms) distributed across the receptive field at the optimal orientation of the cell (Jones and Palmer, 1987b; Cardin et al., 2010). Bars are advantageous in that they activate populations of LGN cells synchronously and generate large postsynaptic potentials (PSPs). The mean ± SD bar width used was 0.4 ± 0.25°. In a subset of cells ($n = 4$), we tailored stimuli pixel by pixel to fall within a subregion as identified by the 2D RF, calculated on-line.

In some cells ($n = 11$), we presented pairs of flashed bar stimuli. We chose two RF locations in adjacent subregions in which to present bar stimuli of the same contrast, such that one bar was excitatory and the other inhibitory. The bars were flashed for 16 ms either individually or simultaneously.

Functional cell classification. Cells were classified as simple or complex based on two criteria, following the study by Cardin et al. (2010). First, the relative modulation of spike trains evoked by an optimized patch of drifting sinusoidal grating was measured. If the response at the fundamental temporal frequency of the stimulus exceeded the average response, the cell was classified as simple. Otherwise, the cell was classified as complex and was not included in the present study. Second, we estimated the one- and/or two-dimensional spatiotemporal weighting functions (see below). Cells exhibiting nonoverlapping regions excited by bright and dark stimuli were classified as simple. Cells exhibiting excitatory responses (V_m depolarization) to bright and dark stimuli throughout their receptive fields were classified as complex. These two measures yielded the same functional classification.

2D RF mapping. In some cells ($n = 8$), the 2D spatiotemporal RF structure was additionally estimated by forward averaging of V_m (spikes removed off-line) with dense 2D noise. We display the estimate of the 2D spatiotemporal weighting function as the average bright correlation minus the average dark for time points up to 300 ms following each frame of visual stimulus, but the separate bright-response and dark-response components demonstrate the true spatial separability of subregions (Fig. 2*A*, right). This measurement allowed comparison of the 2D spatiotemporal receptive field with the 1D spatiotemporal weighting functions (Fig. 1*A*, bottom), and these two metrics were always in close agreement. However, the 2D RF was used only for illustration purposes; in all cases, the optimal orientation used for bar presentations was identified on-line with drifting gratings using a hand-plotting routine.

Spiking and membrane potential analysis. For V_m measurements, spikes were removed by first determining the time at which spike threshold was reached and then extrapolating the membrane potential values from that point to when the spike repolarized back to the spike threshold level. Spike output was quantified in peristimulus time histograms (PSTHs). Firing rates were measured over the first 50 ms of the response.

Following off-line spike removal, the V_m was smoothed with a five-point running average. Measurements of the peak amplitude and timing of V_m responses were made from the average response to a stimulus across all trials. PSP onsets were determined by the peak of the second derivative of the average V_m. For illustration of responses over time and space, pseudocolor plots were generated with bilinear interpolation in both dimensions. In pseudocolor plots of conductances, time points at which excitatory conductance (gE) and inhibitory conductance (gI) were not calculated (see Conductance estimates section below) were represented as having zero gE and gI (light blue).

Conductance estimates. We implemented a method of continuous conductance estimation in which we considered each neuron as a point-conductance model of a single-compartment neuron. The total membrane conductance at each point in time during a visually evoked PSP was calculated, correcting for membrane capacitance, and excitatory and inhibitory components were decomposed, as described extensively previously (Higley and Contreras, 2006; Monier et al., 2008).

Briefly, evoking a synaptic response while holding the cell at multiple V_m levels with varying I_{inj} values gives, for each time point, a current–voltage (*I–V*) plot where the inverse slope of the best line fit is total conductance (gT). We implemented strict linearity criteria (see below) to prevent contamination of the analysis by membrane nonlinearities. Current levels used in *I–V* plots were corrected for capacitive current, which we estimated based on the membrane capacitance of each cell, which was estimated from hyperpolarizing current injections used throughout the experiment.

We calculated resting conductance (gR) as the inverse slope of the *I–V* line of best fit from points averaged from a 40 ms baseline period at stimulus onset (but before cell response onset). This gR value includes both the leak conductance and background synaptic conductances (Monier et al., 2008). Subtracting gR from the gT calculated during the synaptic response gives a measure of the total evoked synaptic conductance (gSyn).

At the synaptic reversal potential ($V_m = V_{rev}$), the synaptic current (I_{syn}) = 0. V_{rev} was therefore calculated as the Y value of the intersection of the baseline *I–V* linear fit with the *I–V* linear fit from each point in the synaptic response. The total synaptic conductance gSyn can then be linearly decomposed into its excitatory and inhibitory components by assuming their Nernst reversal potentials.

We assumed the simplification that the total synaptic conductance is composed of excitatory AMPA conductances and inhibitory $GABA_A$ conductances. Because we were primarily concerned with the fast stimulus-evoked synaptic responses to flashed stimuli, and for the sake of analytical

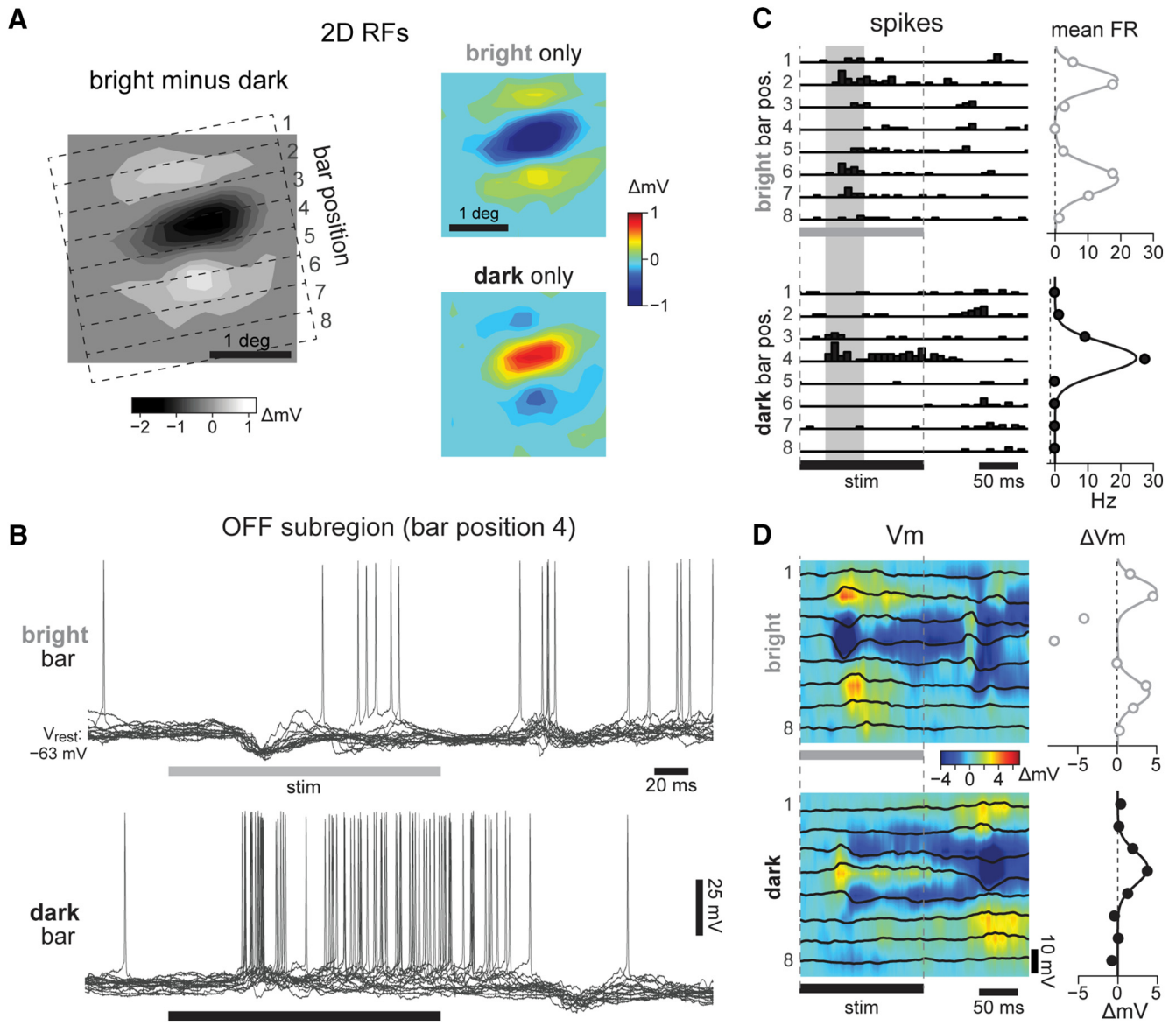

Figure 2. Spatial structure of simple cell receptive fields. ***A***, Left, 2D RF of a simple cell in our dataset, estimated from forward correlation of the V_m at $t = 105$ ms. The RF spanned 2.3° in width, and its optimal orientation was 101°. Dashed lines outline 8 bar positions, each 0.4° wide, used as stimuli for 1D RF characterization. The 2D RF was obtained by subtracting the average V_m responses to dark stimuli (right, bottom) from responses to bright (right, top); red indicates depolarization, and blue indicates hyperpolarization. ***B***, V_m responses to bright (top) and dark (bottom) bars presented in the OFF subregion, at position 4 (16 trials). Horizontal bars, stimulus on time of 160 ms. ***C***, Left, PSTH of spiking responses at each bar position, bright (top) and dark (bottom). Vertical shaded regions show 50 ms window used to calculate response firing rate (FR). Right, Mean FR (points) and Gaussian fits (curves), calculated separately for each RF subregion. ***D***, Left, Average ΔV_m traces (black lines) after off-line spike removal, for all bar positions and contrasts. Pseudocolor maps show interpolation of these traces across time and space. $V_{rest} = -64$ mV. Right, V_m responses at the time of peak response across positions, displayed as in ***C***. Note that the strong hyperpolarization in response to bright bars in the OFF subregion was excluded from the Gaussian fits defining the flanking ON subregions.

simplicity, we assumed negligible contributions of NMDA and $GABA_B$ conductances (Allison et al., 1996; Monier et al., 2008). Reversal potentials for excitation (V_e) and inhibition (V_i) were assumed to be 0 mV and −80 mV, respectively, although varying these values by ±10 mV did not qualitatively impact our results.

Because our estimates of gE and gI are made relative to a resting conductance value that includes background synaptic conductances (Monier et al., 2008), these values are technically ΔgE and ΔgI; for simplicity, we refer to these delta values as gE and gI throughout the article.

Onset latencies of gE and gI were calculated as the time at which each response reached 20% of its peak, and the gSyn onset value was defined as the first onset of gE or gI. Because of the noisiness of conductance estimates, onsets were calculated only for conductances that exceeded 2 nS.

Addressing nonlinearities in conductance estimates. This method of estimating synaptic conductances is susceptible to nonlinearities in the membrane introduced by voltage-gated currents. We implemented several control measures to minimize such contamination. First, in all analyses, depolarizing current levels showing excess spiking and saturation of the V_m were discarded. As a result, the majority of V_m values used in the analysis were below spiking threshold. Furthermore, we imposed a goodness-of-fit criterion of $R^2 > 0.7$ for the linear fit of *I–V* for each time point analyzed; any time point whose fit violated this criterion was discarded from analysis. A careful study comparing voltage-clamp and current-clamp techniques for estimating conductances showed that *in vivo*, the two yield the same conductance estimates (Monier et al., 2008).

Analysis of responses as a function of space. We measured peak responses (V_m depolarization from rest or increase in synaptic conductance) within a 20 ms window across all bar positions for each cell, allowing for some variability in the peak response times between bar positions. These responses were fit to a Gaussian distribution for each RF subregion, and if a cell had

more than two main subregions, we used the two strongest adjacent subregions, defined by V_m depolarization. We limited our analysis to cells for which at least three adjacent bars evoked a conductance response ($n = 18$ cells). Responses over space were well fit by Gaussian distributions; all data met a $R^2 > 0.5$ goodness-of-fit criterion. One cell had only one (ON) subregion and no V_m response to dark stimuli. This cell was discarded from analysis, leaving $n = 17$ cells for our analysis of responses over space.

To compare across the population, distribution parameters (mean and SD) were pulled from the Gaussian fits. Visual space was normalized to 0 at the peak of the V_m response to bright and 1 at the peak V_m response to dark, such that the distance between these centers of adjacent V_m-derived RF subregions defined 1 receptive field unit (RFU). All distributions were normalized to a peak amplitude of 1, except gI was normalized to peak gE to maintain relative magnitudes of gE and gI. Normalization of space was necessary because sometimes the RF of a recorded cell was covered by only a few bar stimuli, whereas in others, all bar stimuli were within the RF. The mean ± SD RFU was 2.5 ± 0.7 bars or 1.0 ± 0.5°.

Among the 33 cells used for subregion analysis, many cells had RFs with two clear subregions, which were counted separately in our analyses, for a total of 56 subregions. Our results are the same whether we average by cell or use all subregions independently.

An alternate method of quantifying responses using the area under the V_m or conductance traces above resting V_m (V_{rest}) or 0, respectively, yielded the same results (data not shown) as the peak method described above.

Simulation of responses to drifting gratings. We generated a drifting sinusoidal stimulus at the cells' ideal spatial frequency (period = 2 RFU) and an arbitrary time scale. The peak values of postsynaptic excitatory and inhibitory conductances to bright and dark stimuli (for cells from our dataset as well as cells from our model, see below) were convolved with each frame of the stimulus, and responses to bright and dark were summed to generate total gE and gI responses to the stimulus over time. V_m responses were generated by convolving the 1D RF with the stimulus. The phase shift of gI relative to gE was quantified as the absolute value of the temporal difference in peaks between the modulated gE and gI responses and was expressed in degrees relative to the full period (360°) of the response to the sinusoidal stimulus.

Model. We simulated a 600 × 25 × 510 μm deep section of L4 in V1, which contained 396 neurons (Beaulieu and Colonnier, 1983), of which 20% were inhibitory (Gabbott and Somogyi, 1986). For simplicity, we assumed that all cells within L4 were simple cells. We simulated simple cell 2D RFs using even- and odd-symmetric Gabor functions (Jones and Palmer, 1987a) with a fixed spatial frequency. RF retinotopic position shifted along the azimuth by 0.5 RF widths per 1 mm along the horizontal plane of L4 (Kremkow et al., 2016a). All cells in the simulation had the same (vertical) orientation preference. We ignored orientation changes for simplicity, since the connections in our model never extended beyond 150 μm (see below). On average, preferred orientation shifts by 15° over 150 μm horizontally (Kremkow et al., 2016a), although depending on the horizontal direction relative to the location of a pinwheel, over >1 mm of cortical distance there may be no significant change in preferred orientation (Bonhoeffer et al., 1995). A 15° shift in preferred orientation falls well inside the half-width at half-height (HWHH) of FS orientation tuning in L4 (25°; Cardin et al., 2007) and is approximately equal to the HWHH for RS cells in L4 (15°; Cardin et al., 2007). Additionally, an intracellular study of functional connectivity between L4 spiny stellate cells found that the majority of connections, and nearly all connections with PSP amplitude >1 mV, were between cells not >100 μm apart laterally (Tarczy-Hornoch et al., 1999). We therefore limited inhibitory connections to cells within 150 μm of each other, and excitatory connections to cells within 100 μm of each other horizontally.

Hebbian plasticity and correlational studies (Michalski et al., 1983; Smith and Kohn, 2008; Denman and Contreras, 2014; Cossell et al., 2015) predict that two excitatory cells with similar visual response properties will be connected. Thus, we considered any two excitatory cells within 100 μm of each other whose RFs were correlated with a value of >0.5 to be functionally connected. The majority of inhibitory neurons in V1 L4 are clutch cells, or small basket cells, whose axonal arborizations densely innervate an ~150 μm radius around their cell bodies without apparent target specificity (Kisvárday et al., 1985; Ahmed et al., 1994, 1997; Binzegger et al., 2004). This is also consistent with connectivity studies of interneurons in other layers and regions of cortex (Fino and Yuste, 2011; Packer and Yuste, 2011). Therefore, we assumed that a simple cell receives input from all inhibitory neurons within a 150 μm radius of its cell body.

We characterized each RF as a 1D function across the center of the 2D RF representing the V_m response to bright minus dark. The firing rate of a cell was a thresholded function of the 1D RF, and the output of FS cells was 10-fold greater than that of RS cells (Contreras and Palmer, 2003). We simulated the excitatory and inhibitory conductances of the postsynaptic cell as the sum of the output of all presynaptic excitatory and inhibitory neurons. The summed responses were fit to a Gaussian. This simulation only generated conductances arising from the local cortical network; inputs from the LGN, other cortical layers, and other brain regions were omitted.

To implement an OFF-anchored RF scheme, we imposed a bias on RF locations as a function of their OFF subregions. An arbitrary location in visual space was chosen to be the center of the OFF-anchor (the "target" OFF location), and each RF was shifted toward that location by a percentage of the distance between the center of the strongest OFF subregion of the RF and the target OFF location.

Experimental design and statistical analysis. All statistical tests were performed in MATLAB (RRID:SCR_001622) and are reported in the Results, along with numbers of cells or measures compared. We used two-sided *t* tests to compare normal distributions. Non-normal distributions were compared using Wilcoxon signed rank tests (noted as "signed rank test") if the data were paired or two-sided Wilcoxon rank sum tests (noted as "rank sum test") for independent measurements. Box plots of population data reflect the following statistics: thick line indicates median, box surrounds 25th to 75th percentile of data, whiskers surround all nonoutlier data, outliers (values >1.5 times the interquartile range greater than or less than the 75th or 25th percentiles, respectively) are sometimes not shown, for clarity; these cases are noted in the figure legends. Plots of averages show the 95% confidence interval as a shaded region surrounding the average. Where appropriate, the Holm method was used to correct significance levels for multiple comparisons, and these are noted in the text.

Results

Simple cell receptive field structure from V_m and spikes

We analyzed the composition of visual synaptic responses of L4 simple cells with intracellular recordings coupled with current injection through the micropipette. The cell in Figure 2 had a 2D RF with a central OFF subregion flanked by two ON subregions (Fig. 2*A*, left). While we represent RFs as the average V_m responses to bright minus dark, responses to each contrast alone show fully separate subregions (Fig. 2*A*, right). Because the procedure for generating 2D RF profiles is slow, it cannot reasonably be combined with the injection of multiple current levels. Consequently, we used 1D stimuli to estimate the gE and gI values underlying the synaptic responses. We used static and brief (128 or 160 ms) bright and dark bars at the optimal orientation of the cell, presented one at a time in 8–16 contiguous positions spanning the width of the RF (Fig. 2*A*, dashed lines). Single trial responses to a bright bar in the OFF subregion of the cell shown in Figure 2 show a consistent phasic hyperpolarization with spike suppression (Fig. 2*B*, top), while the opposite contrast (i.e., a dark bar) in the same position triggered a depolarization leading to sustained spike output (Fig. 2*B*, bottom). This opposite action of bright and dark stimuli on the spike output of the neuron is a typical example of the push–pull nature of the RF subregion (Palmer and Davis, 1981; Ferster, 1988).

The spike output in response to repeated presentations of the bar at all positions was accumulated in PSTHs and revealed the OFF subregion (Fig. 2*C*, bottom, position 4) flanked by two ON

subregions (Fig. 2*C*, top, positions 2 and 6). As in the original push–pull description of simple cell RFs, opposite contrast bars caused the suppression of spike output in the subregions. To obtain a spatial profile of the RF perpendicular to the elongation axis of the subregions, we calculated the integral of the PSTH at each position and fit a Gaussian to each RF subregion (Fig. 2*C*, right). The RF subregions were also well defined by the underlying average V_m after removing action potentials (Fig. 2*D*, black traces and pseudocolor plot) and by the Gaussian fits to the peak ΔV_m from V_{rest} (Fig. 2*D*, right).

Estimation of evoked synaptic conductances

We estimated visually evoked gE and gI from current-clamp recordings by repeating the visual stimulus during several levels of current injection (Fig. 3*A*) and calculating a *I–V* plot at every time point during the response (Fig. 3*B*). The slope of the *I–V* plot yields the R_{in}, and its inverse yields the gT at that point in time. The resting input resistance of this cell was 41 MΩ, and its resting conductance was 24 nS. The comparison of the linear *I–V* relationship at any given point (Fig. 3*A–C*, filled circle) with the linear *I–V* relationship at rest (Fig. 3*A–C*, open circle) yields the total evoked synaptic conductance gSyn and the synaptic reversal potential V_{rev} (Fig. 3*B*; see Materials and Methods). Assuming that the evoked gSyn is composed of AMPAergic excitation ($V_e = 0$ mV) and $GABA_A$ergic inhibition ($V_i = -80$ mV), the gSyn can be decomposed into gE and gI.

The stimulus in Figure 3*A–D* was a dark bar in the OFF subregion of the cell shown in Figure 2. This excitatory stimulus evoked gE reaching a peak magnitude of 6.5 nS and gI reaching a peak magnitude of 17.2 nS (Fig. 3*C*). While concomitant excitation and inhibition have been observed previously, such a large magnitude of gI has not been demonstrated in response to a stimulus expected to be purely excitatory. We performed several types of control experiments and analyses to verify this surprising result.

One potential concern was that this method of conductance estimation is sensitive to nonlinearities in the *I–V* relationship that can arise from intrinsic voltage-activated conductances. Thus, in all analyses, we only included nonsaturating V_m levels, and we discarded any data points that failed a strict linearity criterion. Because action potentials introduce voltage-dependent intrinsic conductances, we

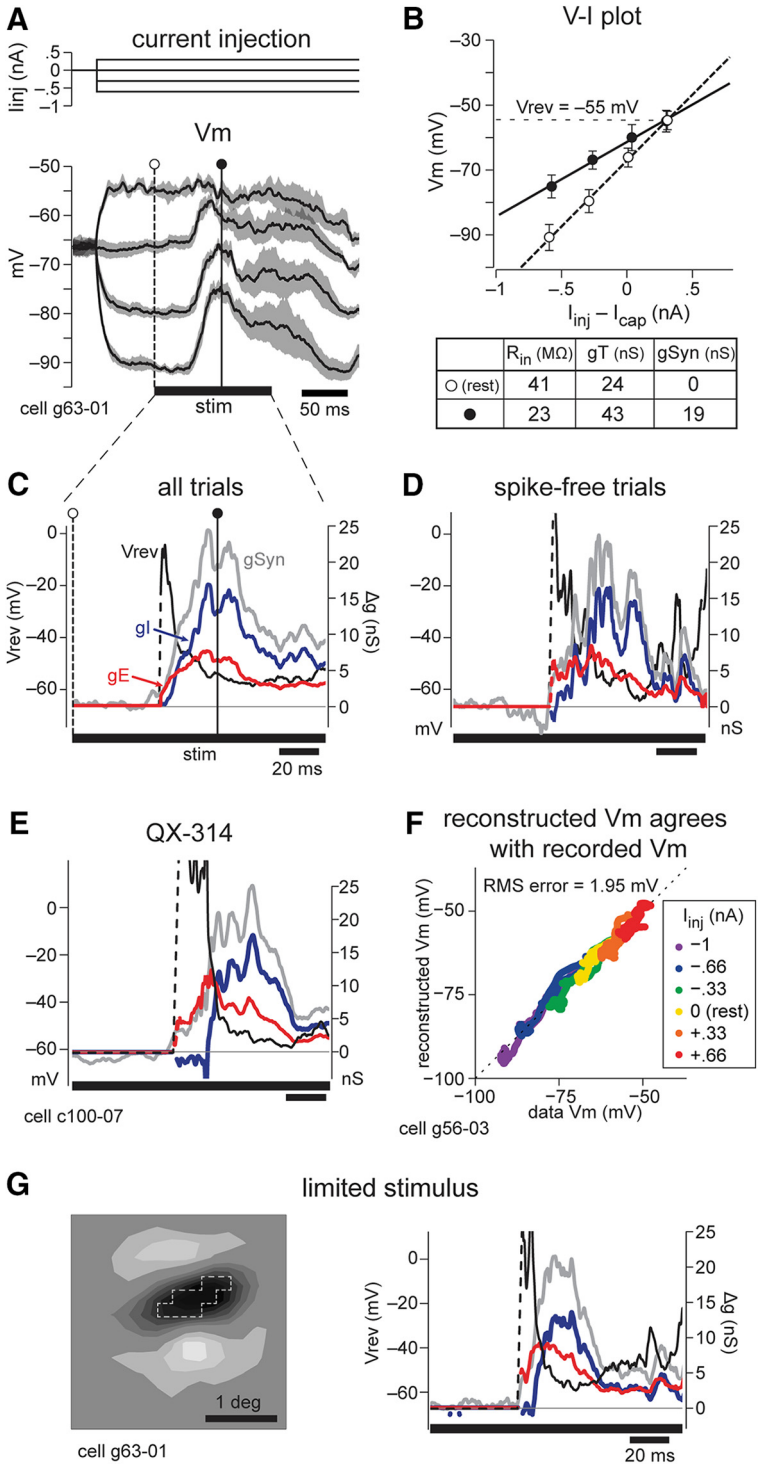

Figure 3. Conductance estimation. ***A***, Top, Levels of current injection through the pipette that were paired with presentations of visual stimuli and used for conductance estimation. Bottom, average ± 95% confidence interval of 12 trials at each of the four levels of current injection. Stimulus on a time of 128 ms shown as the bar under the traces. The time points indicated correspond with points used for the *I–V* plot in ***B*** and are shown in ***C***. ***B***, Linear *I–V* relationship at rest (open circles, dashed line is linear fit, error bars show 1 SD) and at the time point indicated in ***A*** (filled circles, solid line). The slope of each line gives the R_{in}, and the inverse yields total conductance gT. During the synaptic response, gSyn is calculated as gT(*t*) − gT(rest). The intersection of the two lines gives the synaptic reversal potential (V_{rev}) for that time in the response. ***C–E***, ***G***, V_{rev} (black), gSyn (gray), excitatory conductance (gE, red), and inhibitory conductance (gI, blue) as a function of time throughout the synaptic response to the visual stimulus. ***C***, Vertical line indicates the filled circle time point shown in ***A*** and ***B***. ***D***, Analysis using only trials without action potentials. ***E***, An excitatory bar stimulus in a cell recorded with QX-314 in the recording pipette (dark bar in position 7, OFF subregion, of the cell in Fig. 4). ***F***, Time point-by-time point comparison of recorded and reconstructed V_m shows excellent agreement across many levels of current injection, with a root mean square (RMS) error of 1.95 mV. ***G***, Left, A stimulus of dark pixels (outlined in dashed line) was hand plotted on-line to remain well inside the OFF subregion of the cell in ***A–D***. Right, V_{rev}, gSyn, gE, and gI in response to this stimulus.

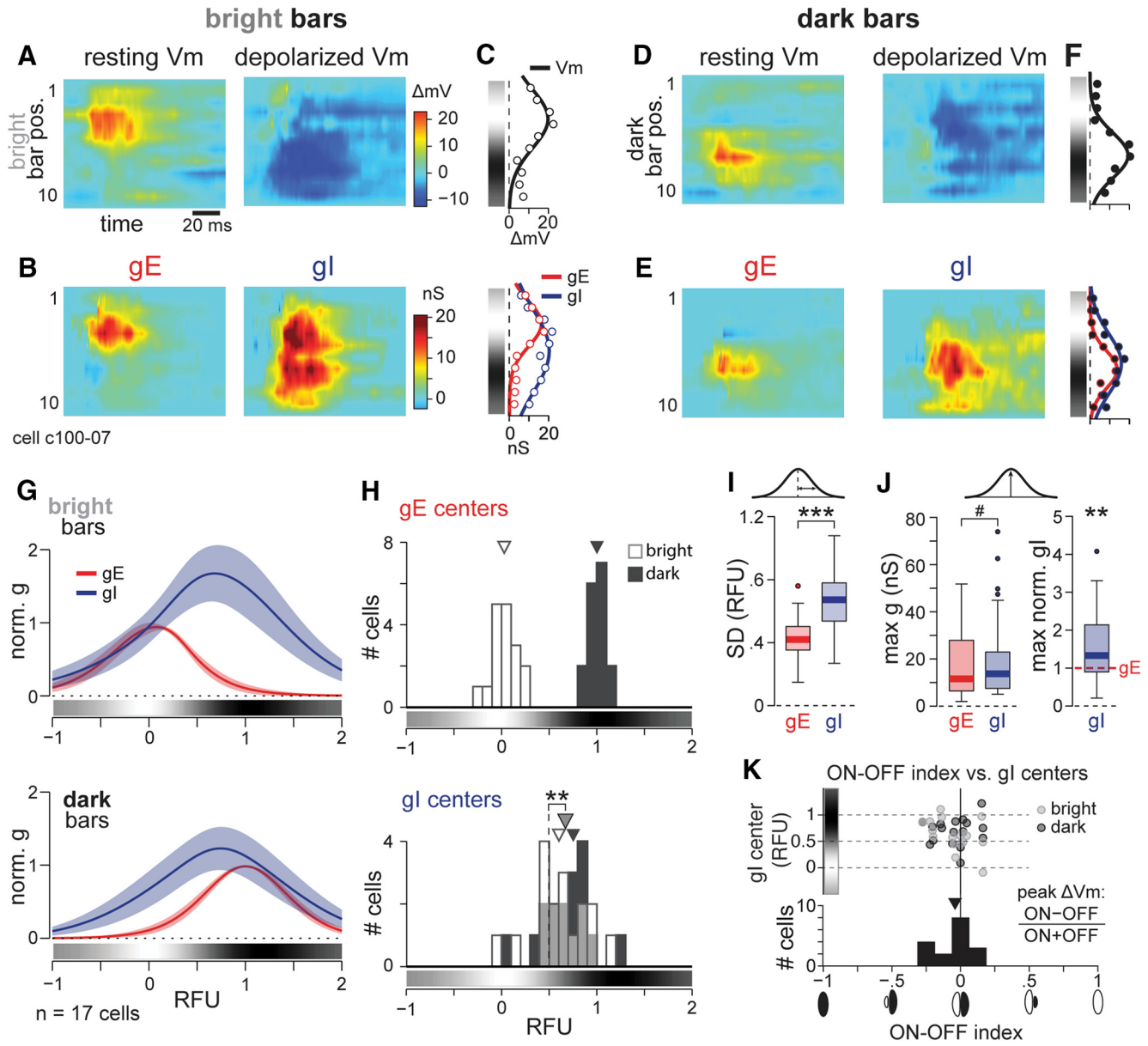

Figure 4. Inhibition is broad across the simple cell RF. ***A***, V_m responses at rest (left, $V_{rest} = -78$ mV) and with depolarizing current (right, $V_{rest} = -41$ mV) of an example simple cell in response to bright bars. Peak depolarization from rest (left) to a bright bar in position 4 was 19.7 mV. ***B***, Left, gE responses to bright stimuli were strictly constrained in space, coinciding with the ON subregions. Right, Bright stimuli evoked strong gI across the width of the RF. ***C***, Gaussian fits of peak resting V_m (top) and gE and gI (bottom) responses to bright bars. Lines are fits; points are data values. Grayscale colorbar representation of the RF shown to the left of each plot was generated from V_m responses as in Figure 1. ***D–F***, as in ***A–C***, but responses to dark bars in the same cell. Peak depolarization from rest (***D***, left) to a dark bar in position 7 was 22.1 mV. ***G***, Mean ± 95% confidence interval of normalized Gaussian fits of gE (red) and gI (blue) responses to bright (top) and dark (bottom) stimuli, $n = 17$ cells. The average 1D RF from V_m responses is shown below each plot. Note that 0 and 1 RFU are defined for each cell as the centers of the ON and OFF subregions, respectively. ***H***, Top, Distributions of the centers of gE responses to bright and dark are segregated by RF subregion ($n = 17$ cells). Bottom, Distributions of the center of gI responses to bright and dark are overlapping. Gray bins show an overlap of the two distributions. Medians are indicated by arrowheads. Centers of all gI responses (median, gray arrowhead) are closer to the OFF than the ON subregions. ***I***, gI responses are broader than gE responses, quantified as SDs of Gaussian fits. ***J***, Left, Absolute values of maximum gE and gI are not quite significantly different for $p < 0.05$. Right, When normalized to maximum gE for each cell and contrast, the maximum gI is on average 1.3 times greater than gE (dashed red line at 1). ***K*** Top, Scatter plot of ON–OFF index versus the centers of gI distributions to bright and dark stimuli. Bottom, The distribution of ON–OFF indices spans zero. Arrowhead indicates median. #$p < 0.06$; **$p < 0.01$; ***$p < 0.001$.

checked whether our method for removing spikes off-line was sufficient to prevent contamination of our analysis. To do this, we estimated conductances using only trials in which the cell fired no spikes; these analyses yielded quantitatively similar results in terms of the dynamics and magnitudes of gE and gI (Fig. 3, compare *D*, *C*).

As a further control, we recorded a subset ($n = 12$) of cells with QX-314 in the recording pipette to block action potentials and voltage-gated potassium and calcium channels (Connors and Prince, 1982; Mulle et al., 1985). We waited until the QX-314 effectively blocked spikes (at least 4 min) before beginning visual stimulation protocols. Excitatory stimulation of an example cell evoked both gE, peaking at 12.1 nS, and gI, peaking at 17.4 nS (Figs. 3*E*, 4, dark bar in OFF subregion of the cell). The analysis of this subpopulation reproduces all of the main results (reported below), suggesting that voltage-gated conductances in the absence of QX-314 did not substantially affect our conclusions about the distribution and time course of synaptic conductances.

We additionally reconstructed the V_m using our derived conductances, assuming a linear membrane regime (Priebe and Ferster, 2005; Monier et al., 2008). The reconstructed V_m values closely matched the recorded values over multiple current injection levels (Fig. 3*F*), which would not be the case if the technique had been contaminated by voltage nonlinearities.

Key to our analysis is the use of optimally oriented bars whose width is smaller than that of the RF subregions. To demonstrate that inhibition was not caused by contamination by adjacent subregions or by end-stopping inhibition, we presented visual stimuli tailored, pixel-by-pixel, to the center of RF subregions (mapped independently with white noise; Fig. 3*G*, left) and obtained the same results (Fig. 3, compare *G*, right, *C*, same cell).

Spatial distribution of responses and synaptic conductances across the RF

The simple cell in Figure 4*A–C* (recorded with QX-314) responded with strong depolarization to bright and dark bars revealing an ON subregion near position 4 (Fig. 4*A*, left) and an OFF subregion near position 7 (Fig. 4*D*, left). Lack of hyperpolarization to bright bars in the OFF subregion (and vice versa) was likely due to low V_{rest} (−78 mV). However, when we injected depolarizing current to bring the V_m up to −41 mV, bright stimuli evoked hyperpolarization across the RF (Fig. 4*A*, right). From the synaptic responses at different V_m levels and all bar positions, we estimated the underlying gE and gI values as a function of space and time. Increases in gE in response to bright bars coincided spatially with the ON subregion (depolarizing V_m responses in positions 2–5), with peak values near the centers of the RF subregions (Fig. 4*B*, left). In contrast, gI was evoked by all bright bar positions (Fig. 4*B*, right), matching the wide distribution of hyperpolarization observed in depolarized V_m trials (Fig. 4*A*, right).

To quantify the spatial distributions of the synaptic response and the underlying gE and gI, we fit a Gaussian to their peak values across all bar positions. The fit of the synaptic response to bright bars, measured as depolarization from rest, defined the ON subregion, which was centered at bar position 3.6 (Fig. 4*C*, top). The fit of gE was centered at bar position 3.4 and had an SD of 1.8 bars, while the fit of gI was centered at bar 5.6 and had an SD of 3.4 bars, almost double the gE SD (Fig. 4*C*, bottom).

We performed the same visualization and analysis of responses to dark bars (Fig. 4*D*,*F*). The center of the OFF subregion was located at bar position 6.9 (Fig. 4*F*, top). gE was spatially limited to the OFF subregion (Fig. 4*E*, left, *F*; gE center at 6.9; SD, 1.6 bars), whereas gI was broadly evoked by dark bars across the RF (Fig. 4*E*, right, *F*; gI center at 6.4; SD, 2.5 bars).

To normalize the spatial dimension of RFs and compare responses across cells with different RF sizes, we defined an RFU as the distance between the peaks of the ON and OFF V_m subregions, which are located at 0 and 1 RFU, respectively (see Materials and Methods; Fig. 4). In the cell in Figure 4*A–F*, 1 RFU = 3.3 bars (~1.4°). We averaged the normalized Gaussian fits of V_m, gE, and gI across all simple cells ($n = 17$). As in the example cell, the population gE was spatially confined to individual subregions, while gI was evoked broadly across the RF (Fig. 4*G*). We measured the broadness of responses over space using the SD of the Gaussian fits, which were 1.6 times greater for gI than for gE [Fig. 4*I*; median SD, gE = 0.42 RFU, gI = 0.67 RFU; gE vs gI: $Z = 4.74$, $p = 2.1 \times 10^{-6}$, $n = 34$ responses (bright and dark) from 17 cells, signed rank test]. The subset of cells recorded with QX-314 showed the same wide distribution of gI relative to gE (QX-314: median SD, gE = 0.43 RFU, gI = 0.65 RFU; gE vs gI: signed rank = 101, $p = 8.5 \times 10^{-4}$; $n = 14$ responses from 7 cells, signed rank test).

Furthermore, the centers of evoked gE in the population were very close to the corresponding V_m-defined ON and OFF subregion centers (Fig. 4*H*, top; median gE center to bright = 0.03 RFU; median gE center to bright to dark = 1.0 RFU). Spatially restricted inhibition would predict evoked gI centered at and limited to the opposite contrast RF subregion (Fig. 1*B*). Instead, a population gI distributions to both contrasts were centered close to each other, reflecting their largely overlapping responses to bright and dark (Fig. 4*H*, bottom; median gI center to bright = 0.60 RFU; median gI center to dark = 0.75 RFU; population gI centers to bright vs dark: $t_{(16)} = 0.85$, $p = 0.41$, $n = 17$, paired t test). The subset of cells recorded with QX-314 also had overlapping gI responses to bright and dark (QX-314: median gI center to bright = 0.60 RFU; median gI center to dark = 0.51 RFU; bright vs dark: $t_{(6)} = -0.45$, $p = 0.65$, $n = 7$, paired t test).

Surprisingly, the population gI distributions to both contrasts were centered significantly closer to the OFF subregion than the ON subregion (Fig. 4*H*, bottom, large gray arrowhead indicates population median of 0.67, different from 0.5, $t_{(33)} = 3.2$, $p = 0.003$, $n = 34$ responses, two-sided t test). One possible explanation for this result could be that the RFs of these simple cells were dominated by OFF subregions. To test for this possibility, we calculated an ON-OFF index for each cell from the peak V_m depolarizations from rest from the strongest ON and OFF subregions in each cell: [ON − OFF]/[ON + OFF]. A negative ON-OFF index would indicate stronger V_m responses to dark (OFF-dominated cell), while a positive value would indicate an ON-dominated cell. The distribution of ON-OFF indices ranged from −0.28 to +0.16 and was centered at zero, indicating that our population of simple cell RFs did not have stronger OFF subregions overall (Fig. 4*K*, lower histogram; median = −0.04, not significantly different from zero: $t_{(16)} = -1.35$, $p = 0.197$, $n = 17$, two-sided t test). There was no correlation between ON-OFF index and gI centers (Fig. 4*K*, top scatter plot).

The peak values of population gI across the RF in response to either contrast were approximately equivalent to or greater in magnitude than those of gE [Fig. 4*J*, left; median peak gE = 11.6 nS, gI = 13.7 nS; gE vs gI: $Z = -1.89$, $p = 0.059$, $n = 34$ responses (bright and dark) from 17 cells, signed rank test]. When normalized to maximum gE, maximum gI was 1.3 times greater than gE (Fig. 4*J*, right; $Z = -3.03$, $p = 0.0024$, $n = 34$, signed rank test). The subset of cells recorded with QX-314 also revealed similar magnitudes of gE and gI [QX-314: median peak gE = 15.2 nS, gI = 12.9 nS; gE vs gI: $Z = 0.34$, $p = 0.72$, signed rank test, $n = 14$ responses (bright and dark) from 7 cells]. Since gI was spatially broad, gE and gI appeared comparable in magnitude at the subregion centers defined by V_m (Fig. 4*G*). In addition, peak values of gI from bright and dark were not significantly different, although bright-evoked gI trended toward being significantly greater than dark-evoked gI (median peak gI to bright gI = 16.4 nS, median peak gI to dark = 12.5 nS, $Z = 1.73$, $p = 0.084$, $n = 17$ cells, rank sum test). Across the widths of simple cell RFs, therefore, inhibition was evoked from much of the RF but was centered closer to OFF subregions, whereas excitation was sharply localized to RF subregions.

Broad inhibition generates diverse phases of gE and gI in response to drifting gratings

Although we did not estimate synaptic conductances evoked by drifting gratings in our *in vivo* recordings, we simulated responses to drifting gratings using the spatial maps of gE and gI evoked by

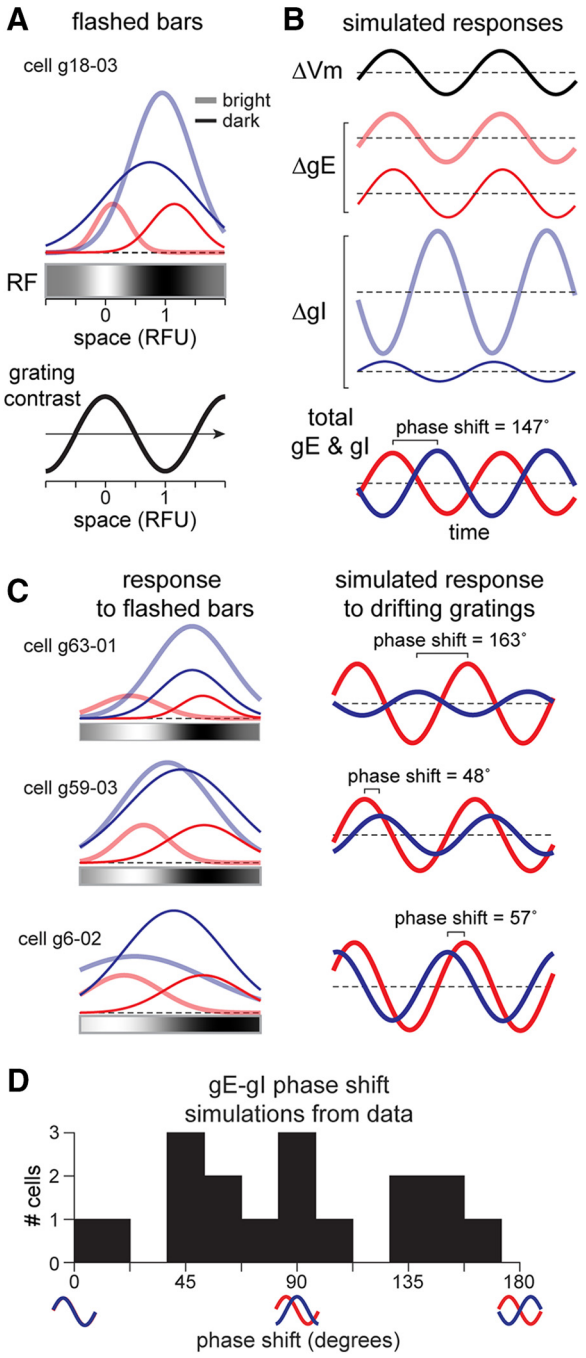

Figure 5. Broad inhibition can generate a diversity of phase shifts of gE and gI modulation to gratings. ***A***, Top, Peak gE and gI responses (Gaussian fits) evoked by bright and dark stimuli across the RF, as in Figure 4, and 1D RF from V_m. Bottom, Single "frame" of sinusoidally varying contrast (grating) used in the simulations in this figure. Arrow indicates direction of drift. ***B***, Top, Simulated V_m response was generated by convolving the 1D RF from V_m with the stimulus at each point in time. Middle, The bright-evoked and dark-evoked gE and gI responses were similarly generated by convolving their spatial distributions with the drifting grating stimulus. Bottom, Total gE and gI responses to the drifting grating stimulus, with a phase shift between gE and gI of 147°, close to antiphase. ***C***, Three more examples, all with broad inhibition but with varying levels of gE– gI phase shift. ***D***, The spatial distributions of gE and gI estimated in the $n = 17$ cells in our dataset produce a diverse set of simulated gE– gI phase shifts.

flashed bars. Another example of peak conductance responses to bars in a simple cell is shown in Figure 5*A*, with typically broad and OFF-subregion biased inhibition. We generated the drifting grating stimulus using sinusoidally varying contrast (Fig. 5*A*, bottom) with spatial frequency of 2 RFU to optimally stimulate each cell and that shifted in visual space with each time step. The stimulus at each point in time was convolved with the 2D RF of the cell to generate an estimate of the V_m response of the cell over time (Fig. 5*B*, top). Convolution of the stimulus with the fit peak bright- and dark-evoked gE and gI generated the bright and dark responses over time (Fig. 5*B*, middle). These were summed to generate total simulated gE and gI in response to the grating (Fig. 5*B*, bottom). In this cell, despite overall broad inhibition, drifting gratings caused a near-antiphase temporal modulation of gE and gI (phase shift, 147°). While these simulations do not take into account the temporal dynamics of the responses to flashed stimuli, including relative delays and time courses of gE and gI, they provide a useful conceptual understanding of how broad inhibition might generate antiphase gE and gI in response to gratings.

The spatial distributions of gE and gI in response to flashed bars for three other example cells are shown in Figure 5*C* (left column), along with their simulated responses to the drifting grating (Fig. 5*C*, right column). These simulations showed a diversity of phase shifts between gE and gI. The simulated responses of all 17 cells in our dataset produced a wide variety of gE–gI phase shifts (Fig. 5*D*). The modulation of gI in response to gratings is strongest when the distributions of bright- and dark-bar evoked gI values are different in magnitude or center location (Fig. 5*A–C*). This gI modulation tends to be antiphase to gE when the bright-evoked gI is strongest near the OFF subregion, which is reminiscent of a push–pull organization of inhibition, although the distributions are still broad. In summary, small differences in the distributions of gI to bright and dark generate modulated gI in response to a drifting grating, while small differences in the distributions of gE and gI lead to a variety of temporal phase differences to gratings, which is compatible with published data (Anderson et al., 2000; Monier et al., 2008; Tan et al., 2011).

Synaptic conductances at RF subregion centers

So far, we have defined the spatial profile of gE and gI across the full width of the RF. However, the push–pull organization of simple cell RFs is defined by opposing responses to bright and dark stimuli within a single RF subregion. To study the magnitude and time course of gE and gI in individual subregions, we focused our analysis on bar stimuli presented at the subregion centers, for a total of 56 subregions (30 ON, 26 OFF) from 33 simple cells.

Across the population, excitatory stimuli in ON and OFF subregions evoked membrane depolarizations and firing rate increases of comparable amplitude and latency. The median peak depolarization from bright bars in ON subregions was 11.7 mV (Fig. 6*A*, top left; $n = 30$), while from dark bars in OFF subregions was 12.7 mV (Fig. 6*A*, top right; $n = 26$). Excitatory stimulation of OFF subregions did not evoke greater depolarization or more spikes than ON subregions (Fig. 6*A*, top: V_m: $Z = -0.04$, $p = 0.96$, rank sum test; Fig. 6*A*, middle: spikes: $Z = 0.60$, $p = 0.55$, rank sum test), which further confirms that our population of simple cells did not have either ON- or OFF-dominated RFs. The underlying peak gE was also comparable (Fig. 6*C*; median peak gE, bright-ON = 9.9 nS, $n = 30$; dark-OFF = 8.6 nS, $n = 26$; $Z = 0.16$, $p = 0.88$, rank sum test). Finally, as shown in Figure 3 and implied from the broad inhibition shown in Figure 4, excitatory stimuli evoked gI of comparable magnitude to that of gE (Fig. 6*A*, bottom row). The peak gI elicited by these excitatory stimuli was similar in both ON and OFF subregions and was not statistically different from peak gE (Fig. 6*C*; median peak gI, bright-ON = 8.2 nS, $n = 30$; dark-OFF = 12.0 nS, $n = 26$; gI ON vs OFF: $Z = -0.52$, $p = 0.60$, rank sum test).

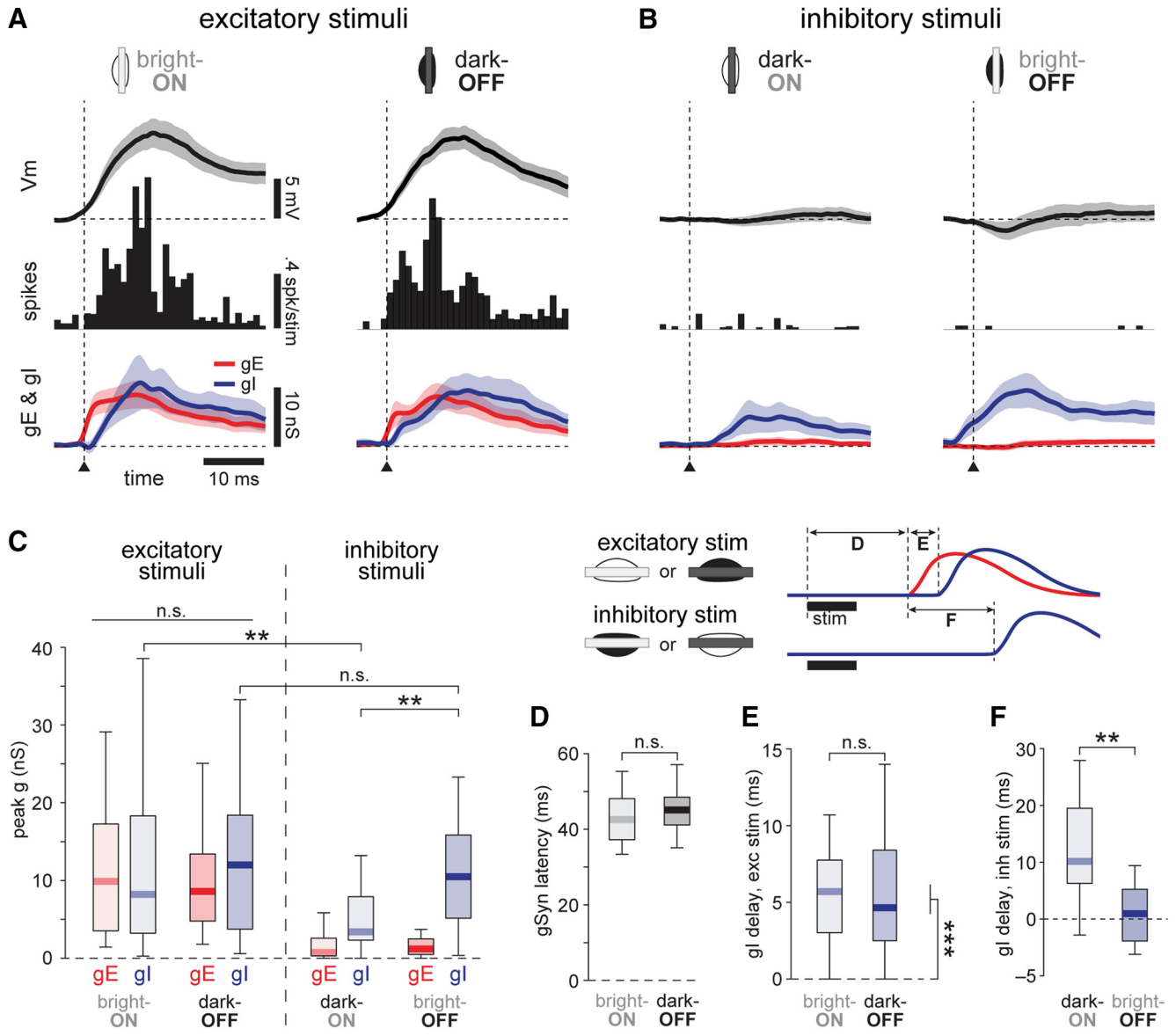

Figure 6. Dynamics of conductances from stimuli at RF subregion centers. ***A***, Responses to excitatory stimuli. Left column, Bright bars in ON subregions; right column, dark bars in OFF subregions. Top row, mean ± 95% confidence interval of ΔV_m from rest. Middle row, Average PSTH from cells recorded without QX-314. Bottom row, average estimated gE (red) and gI (blue) underlying the V_m and spiking responses. Arrowhead and vertical dashed line indicate synaptic response onset, to which responses were aligned before averaging. ON subregions: V_m and conductances, $n = 30$; spikes, $n = 19$. OFF subregions: V_m and conductances, $n = 26$; spikes, $n = 17$. ***B***, Same as ***A***, but for inhibitory stimuli: dark bars in ON (left) and bright bars in OFF (right) subregions. Note that the onset time for these plots is derived from the response onset to the corresponding excitatory stimulus in the same subregion (***A***). Differences in relative response times of gI are quantified in ***F***. ***C***, Peak conductances from the data in ***A*** and ***B***. There were no differences between peak gE and gI for ON and OFF subregions (all p values >0.025 significance level corrected for multiple comparisons). Peak dark-ON gI was less than bright-OFF gI, and also was less than bright-ON gI. Outliers are not shown in boxplots. ***D–F***, Latencies of conductances, measured as illustrated in the inset above. Outliers not shown in boxplots. ***D***, Onset latency of the synaptic response for ON and OFF subregions. ***E***, For excitatory stimuli, onset delay between gE and gI was significant, but did not differ between ON and OFF subregions. ***F***, For inhibitory stimuli, onset delay of gI, measured relative to gE onset from an excitatory stimulus in the adjacent subregion, was greater for dark bars than bright bars, $n = 22$. **$p < 0.01$; ***$p < 0.001$.

Inhibitory stimuli (the opposite contrast in the same subregions) evoked mild or no hyperpolarization (Fig. 6*B*; median hyperpolarization: dark-ON = −1.0 mV, bright-OFF = −1.8 mV; $Z = 1.11$, $p = 0.27$, rank sum test). Despite suppressing spike output, inhibitory stimuli elicited a small gE (Fig. 6*B*,*C*; median peak gE: dark-ON = 0.74 nS, bright-OFF = 1.2 nS), which was swamped by strong gI (Fig. 6*B*, bottom). Although there was no significant difference in hyperpolarization between ON and OFF subregions, bright bars in OFF subregions evoked significantly greater gI than dark bars in ON subregions (Fig. 6*B*, bottom, *C*; median peak gI: dark-ON = 3.4 nS, bright-OFF = 10.5 nS; ON vs OFF: $Z = -2.92$, $p = 0.0035$, rank sum test, significant at 0.025 level for multiple comparisons).

Surprisingly, a comparison of the amplitudes of gI from excitatory and inhibitory stimuli (see above) reveals that excitatory stimuli triggered greater or equal gI than inhibitory stimuli (Fig. 6*C*; median peak gI, OFF subregion, bright vs dark: $Z = 1.11$, $p = 0.27$, signed rank test; median peak gI, ON subregion, bright vs dark: $Z = 3.40$, $p = 6.6 \times 10^{-4}$, signed rank test, significant at 0.025 level for multiple comparisons).

Onset delays between excitation and inhibition

An advantage of using brief presentations of stimuli is that we can analyze the time course of the visual responses. In the time domain, the onset latencies of synaptic responses to excitatory stimuli in ON and OFF subregions were not different (Fig. 6*D*; median latency,

ON = 42.6 ms; OFF = 45.1 ms, $Z = -1.09$, $p = 0.27$, rank sum test). However, the onset of gI was delayed with respect to gE by 5.4 ms (median; significantly different from zero, $Z = 5.35$, $p = 8.6 \times 10^{-8}$, $n = 56$, signed rank test). The delay was similar for excitatory responses in both ON and OFF subregions (Fig. 6*E*; gE-gI onset delay, ON = 5.7 ms, OFF = 4.7 ms; ON vs OFF: $Z = 0.25$, $p = 0.80$, rank sum test). Thus, despite driving robust spike output, excitatory stimuli in ON and OFF subregions evoked balanced levels of excitation and inhibition, with a delay between gE and gI onset.

As discussed above, gI is triggered both by excitatory and inhibitory stimuli, and thus a bright or dark stimulus spanning the entire RF will trigger gI from ON and OFF subregions, functionally suppressing the spike output of the cell (Hubel and Wiesel, 1959). How these two sources of gI combine to contribute to spike suppression depends on the relative delays to gE onset. Therefore, we analyzed responses to a bar of the same contrast presented in adjacent subregions: by definition, one position is excitatory and the other inhibitory. For a bright bar, gI in the OFF subregion was not delayed but started at the same time as gE in the ON subregion (Fig. 6*F*, right; median onset delay = 0.95 ms, not different from zero: $Z = 0.60$, $p = 0.55$, $n = 22$ cells, signed rank test). In contrast, for a dark bar, gI from the ON subregion began 10.2 ms later than gE from the OFF subregion (Fig. 6*F*, left; different from zero, $Z = 3.51$, $p = 4.6 \times 10^{-4}$, signed rank test; bright vs dark bars, $Z = -2.94$, $p = 0.0033$, signed rank test).

Thus, because the spatial distribution of inhibition is biased toward the OFF subregion (Fig. 4), it follows that an inhibitory stimulus elicits stronger inhibition in OFF compared with ON subregions (Fig. 6*B*,*C*). We furthermore show that inhibition in OFF subregions is evoked earlier than that in ON subregions (Fig. 6*F*). Together, these results suggest a functional difference in spatial integration of bright and dark stimuli, which we explored next.

Spatially opponent inhibition determines spatial input integration

To assess differences in spatial integration due to stimulus contrast, we presented bar pairs of the same contrast placed in neighboring subregions (two bright bars, $n = 7$; two dark bars, $n = 5$). In the simple cell in Figure 7, *A* and *B*, a bright bar presented alone elicited a 9.1 mV depolarization in the ON subregion and a 6.9 mV hyperpolarization in the adjacent OFF subregion. Simultaneous presentation of the two antagonistic stimuli led to an approximately linear summation of the responses: a small 0.6 mV depolarization relative to the original baseline, representing a 92% suppression of the response to the bright bar alone. The spiking response of the cell was suppressed by 90%, from 24.6 to 2.4 Hz (Fig. 7*B*, bottom).

In the cell in Figure 7*C*, a dark bar presented alone in the OFF subregion elicited a depolarization of 12.2 mV, and when presented in the ON subregion, it did not trigger a hyperpolarization. However, simultaneous presentation of the two bars reduced the synaptic response to 7.1 mV (42% suppression), a signature of shunting inhibition (Frégnac et al., 2003). The spike output was reduced from 28.3 to 6.9 Hz (Fig. 7*C*, bottom). This suppression of 76% was the strongest spike suppression we recorded with two dark bars. Shunting inhibition was not specific to dark stimuli or OFF subregions, as we also observed shunting responses to bright bars (Fig. 7*D*).

Across the population, bright stimuli caused a median 30% suppression of depolarizing responses, compared with 11% suppression from dark stimuli [Fig. 7*E*, left; bright vs dark suppression, rank sum = 53, $p = 0.27$, $n = 7$ (bright) and $n = 5$ (dark), rank sum test]. This difference was amplified by the spike threshold, leading to a large and significant difference in the suppressive effect of bright (93%) versus dark (40%) bars in the spike output [Fig. 7*E*, right; bright vs dark suppression of firing rate: rank sum = 61, $p = 0.010$, $n = 7$ (bright) and $n = 5$ (dark), rank sum test]. Thus, we established that a single inhibitory bright bar stimulus in an OFF subregion is twice as effective at suppressing spiking responses as an inhibitory dark bar in an ON subregion, as predicted by OFF subregion-biased inhibition (Figs. 4, 6).

Fast-spiking cells do not differ from regular-spiking cells in synaptic RF structure

Given the spatially broad inhibitory input shown above, we investigated the RFs of inhibitory simple cells to determine whether their RFs were broader than those of excitatory cells. We characterized 1D RFs from RS ($n = 10$), FRB ($n = 2$), and FS ($n = 5$) simple cells (RS and FRB cells are putatively excitatory cells, FS cells are putatively inhibitory), based on spike width (Fig. 8*A*) and firing characteristics (see Materials and Methods). This proportion of putatively inhibitory cells (~30%) exceeds the proportion reported by anatomy (20%; Gabbott and Somogyi, 1986) because these cells were selected from a larger subset of recordings, and we only included recordings that were stable for long enough to complete the necessary visual stimulus and current injection protocols. In our hands, FS cells tend to provide more stable recordings, which likely explains their relative overrepresentation in this dataset. We did not include complex cells in this manuscript (see Materials and Methods and Discussion).

We found that the RFs of RS, FS, and FRB simple cells have similar size and structure, as well as similar spatial and temporal distribution of gE and gI (Fig. 8). The average RFU for FS cells ($1.1 \pm 0.2°$, $n = 5$) was not significantly different from that of RS and FRB cells ($1.0 \pm 0.3°$, $n = 12$; $p = 0.63$, rank sum test), indicating that overall RF sizes were not different between cell types. The ON-OFF indices of the five FS cells ranged from −0.20 to +0.15, with a median of −0.05 (not significantly different from zero: $t_{(4)} = -0.48$, $p = 0.66$, *t* test, $n = 5$), indicating that like the full population of simple cells in this study, FS cells did not have OFF-dominated RFs.

The cell in Figure 8*B–F* is a typical FS cell, with nonadapting spike trains at frequencies exceeding 400 Hz in response to visual stimulation, a spike duration of 0.6 ms measured at the base and a pronounced afterhyperpolarization (Fig. 8*B*). The RF had two main subregions (Fig. 8*C*, 148° orientation, 2.8° width), although the OFF subregion was stronger than the ON subregion (ON–OFF index = −0.2). The cell responded robustly to a dark bar presented in the center of its OFF subregion, with a peak gE of 28 nS and peak gI of 47.5 nS (Fig. 8*D*; gE–gI delay = 10.3 ms). A bright bar in the same position (Fig. 8*E*) caused a 2.0 mV hyperpolarization caused by an increase in gI reaching 29.3 nS with negligible gE. The median delay between gE and gI in response to an excitatory stimulus for all FS subregions (5.4 ms, $n = 11$) was indistinguishable from that of RS and FRB subregions (5.3 ms, $n = 37$; FS vs RS/FRB: $Z = -0.15$, $p = 0.87$, rank sum test).

In this cell, the patterns of gE and gI in response to bright and dark stimuli matched the full population of simple cells in Figure 4: gE was spatially restricted to the RF subregions, while gI was broad and centered closer to the OFF subregion (Fig. 8*F*; center ± SD: gE, bright stimuli = 6.1 ± 0.99 bars or 0.17 ± 0.35 RFU; gE, dark stimuli = 3.8 ± 0.78 bars or 0.99 ± 0.27 RFU; gI, bright = 4.6 ± 1.5 bars or 0.77 ± 0.52 RFU; gI, dark = 4.4 ± 1.56 bars or 0.78 ± 0.55 RFU).

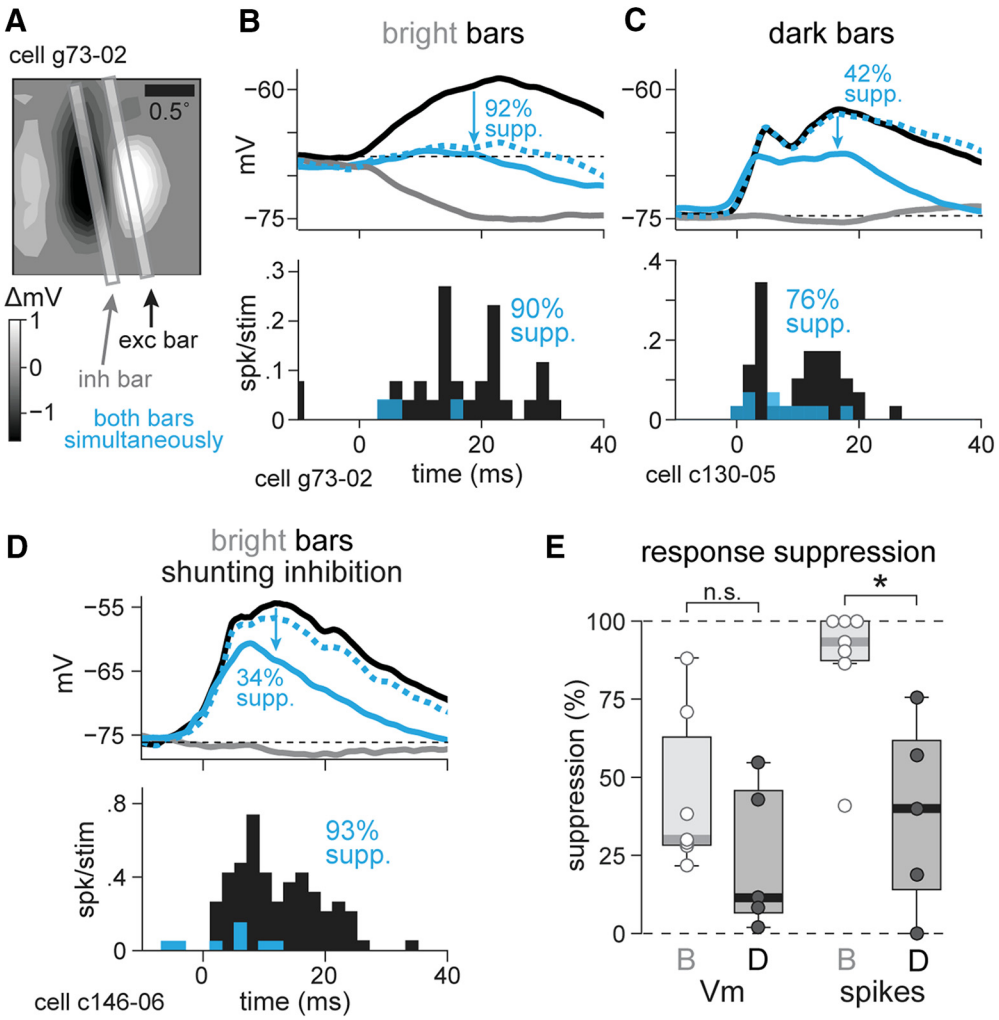

Figure 7. Bright inhibitory bars suppress spikes more efficiently than dark inhibitory bars. ***A***, Example 2D RF and corresponding bar stimuli used for suppression experiment. The bright bar in the ON subregion is the excitatory stimulus, whereas the bright bar in the OFF subregion is inhibitory. The bars were presented individually and simultaneously. ***B***, Top, V_m responses in the cell from ***A*** to the excitatory bright bar alone (black), the inhibitory bright bar alone (gray), and the combined stimulus (solid cyan), as well as the algebraic sum of the two individual stimuli (dashed cyan). The depolarization in response to the combined stimulus represents a 92% suppression (supp.) of the peak depolarization from the excitatory stimulus alone. Bottom, PSTH of spikes in response to the excitatory bright bar alone (black bars) and to the combined stimulus (cyan), showing a 90% suppression of spikes. ***C***, As in ***B***, an example with dark bars. ***D***, As in ***B***, an example with shunting inhibition from bright bars. ***E***, Suppression of peak depolarization (left) and spikes (right) from $n = 7$ cells stimulated with bright bars and $n = 5$ cells with dark bars. While the difference in the suppression of depolarization between bright and dark bar stimuli did not reach statistical significance, spike suppression was significantly less effective for dark bars than for bright bars. *$p < 0.05$.

The average Gaussian fits of gE and gI of the five FS cells were similar to those of the full population of simple cells, with broad inhibition centered closer to the OFF subregion (Fig. 8*G*; median center of gI = 0.68 RFU, significantly different from 0.5: $t_{(9)} = 2.60$, $p = 0.029$, $n = 10$, paired t test). The SDs of gI were 1.6 times broader than those of gE (median SD: gE = 0.41 RFU, gI = 0.67 RFU; gE vs gI: signed rank = 52, $p = 0.0098$, $n = 10$, signed rank test). Maximum gE and gI for each cell were not significantly different.

An analysis of maximum conductance values evoked at subregion centers revealed that FS cells had significantly higher gSyn values compared with RS and FRB cells (median peak gSyn for RS/FRB = 11.0 nS, $n = 45$; FS = 34.0 nS, $n = 11$; $Z = -2.6$, $p = 0.0088$, rank sum test). Consistent with a previous study in the somatosensory system (Cruikshank et al., 2007), magnitudes of gE and gI were greater in FS than in RS cells. However, the spatial and temporal response patterns of gE and gI matched the full population of simple cells, as described above. Our overall findings are the same whether we include all cell types or only include RS/FRB cells. Thus, we included all simple cells, regardless of electrophysiological class, in our population analyses.

Nonspecific inhibitory–excitatory connectivity generates broad inhibition and modulated gE and gI to gratings

If the RFs of FS cells are not broader than those of RS cells, how is spatially broad inhibition generated in L4? We hypothesized that broad inhibition simply results from the known wiring diagram for L4 of V1. Inhibitory interneurons in V1 L4 primarily consist of small basket cells (or clutch cells; Ramón y Cajal, 1909; Kisvárday et al., 1985; Somogyi and Soltész, 1986), which have dense axonal arborizations within a 150 μm radius of their cell bodies. Interneurons in other cortical layers and regions have very dense, if not complete, connectivity within this distance (Fino and Yuste, 2011; Packer and Yuste, 2011). The most reasonable assumption given the anatomy is that inhibitory cells connect indiscriminately to nearby cells in L4, regardless of their RF properties. As a consequence, inhibition disregards the RF of the postsynaptic cell (Fig. 9*A*). Note that the inhibition for an individual cell pair may be spa-

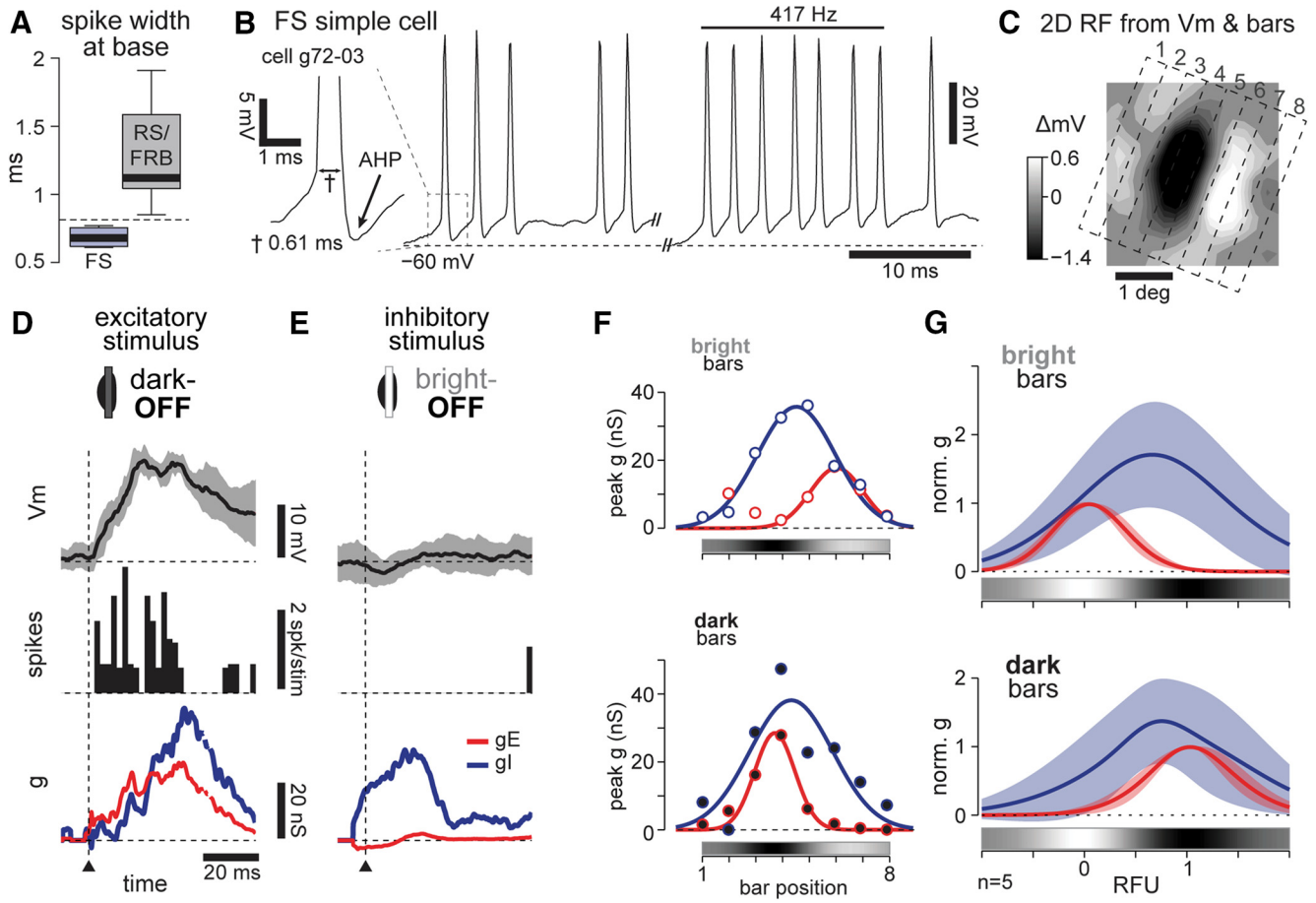

Figure 8. FS cell RFs are indistinguishable from RS cells. ***A***, Average width at spike base for the $n = 5$ FS cells and $n = 11$ RS and FRB cells used for comparisons in this figure. Dashed line at 0.8 ms cleanly divides the two groups. ***B***, Spiking response examples from an FS cell. Left inset, Thin spike (0.6 ms at base) and large afterhyperpolarization (AHP). Right, Bursts of high-frequency, nonadapting spikes in response to visual stimuli. ***C***, 2D RF and bars (dotted lines) used as 1D stimuli. ***D***, V_m (mean ± 95% confidence interval from 6 trials), spiking, and conductance responses to a dark excitatory stimulus in the OFF subregion of the cell from ***B***, as in Figure 5*B*. $V_{rest} = -75$ mV. ***E***, As in ***D***, responses to a bright inhibitory stimulus in the same OFF subregion. ***F***, Peak gE and gI responses to bright and dark stimuli across the RF, as in Figure 4. 1D colorbars show subregions defined by the V_m. ***G***, Average gE and gI fit responses over space for 5 FS cells in our dataset.

tially antiphase in only a minority of cases, when the presynaptic and postsynaptic cell RFs happen to be anticorrelated (Fig. 9*A*, cell E1).

Given the above assumption, it follows that a population of inhibitory presynaptic cells with varying RFs will generate a footprint of summed inhibition on their postsynaptic target that broadly covers the full RF (Fig. 9*B*), which is in agreement with our experimental findings. We tested this hypothesis by creating an anatomy-based model of a small volume of V1 L4 using published anatomical and physiological data and very few assumptions (see Materials and Methods). The essential elements of the model are the proportions of excitatory (80%) and inhibitory (20%) neurons in cat L4 and the promiscuous nature of synaptic contacts of inhibitory neurons within a 150 μm radius of their axonal arborizations. Each RF was randomly drawn from four phases of simple cells, and RF locations in visual space shifted by 0.5 RF widths/1 mm in the horizontal plane of L4 (Kremkow et al., 2016a). Correlation studies suggest that local excitatory connections are limited to neurons with similar functional response properties and RFs (Smith and Kohn, 2008; Denman and Contreras, 2014; Cossell et al., 2015), so excitatory input from the local network should coincide with that of the LGN and be limited to the RF subregions. For simplicity, we assumed equal synaptic weights for all connections, but a version of the model with exponentially decaying weights as a function of distance between the cell pair yielded the same results (data not shown).

An example simple cell from this model (Fig. 10*A*, red star) received excitatory input from cells within a horizontal distance (or column) of 100 μm and with an RF spatial correlation of >0.5 (Fig. 10*A*, black circles with X, *C*, left; see Materials and Methods). Inhibitory input originated from all inhibitory cells within a radius of 150 μm (Fig. 10*A*, blue circles with X). Therefore, inhibitory presynaptic cell RFs largely overlapped in space with but had random correlation of phase relative to the postsynaptic cell as illustrated by a subset of inhibitory neurons in Figure 10*B*. The 1D RFs of all presynaptic excitatory and inhibitory neurons for the example cell are represented in Figure 10*C*. For simplicity, orientation changes were not considered, since within 100–150 μm average changes in orientation are within the HWHH of orientation tuning (see Materials and Methods).

Thus, the population of excitatory cells presynaptic to the example postsynaptic cell had very similar RFs (Fig. 10*C*, left), while the presynaptic inhibitory cell RFs varied substantially (Fig. 10*C*, right). The resulting responses to bright and dark stimuli formed small, spatially localized distributions of excitation (Fig. 10*D*, left) and larger, broad inhibition (Fig. 10*D*, right). Gaussian fits to the simulated gE and gI reproduced the broadness of gI relative to gE (Fig. 10*D*,*E*). However, under the conditions of this simulation there was no bias of gI toward the OFF subregion (Fig. 10*F*; simulation: gI centers median = 0.54 RFU; not significantly different from 0.5, $p = 0.77$, $n = 157$ cells, signed rank test).

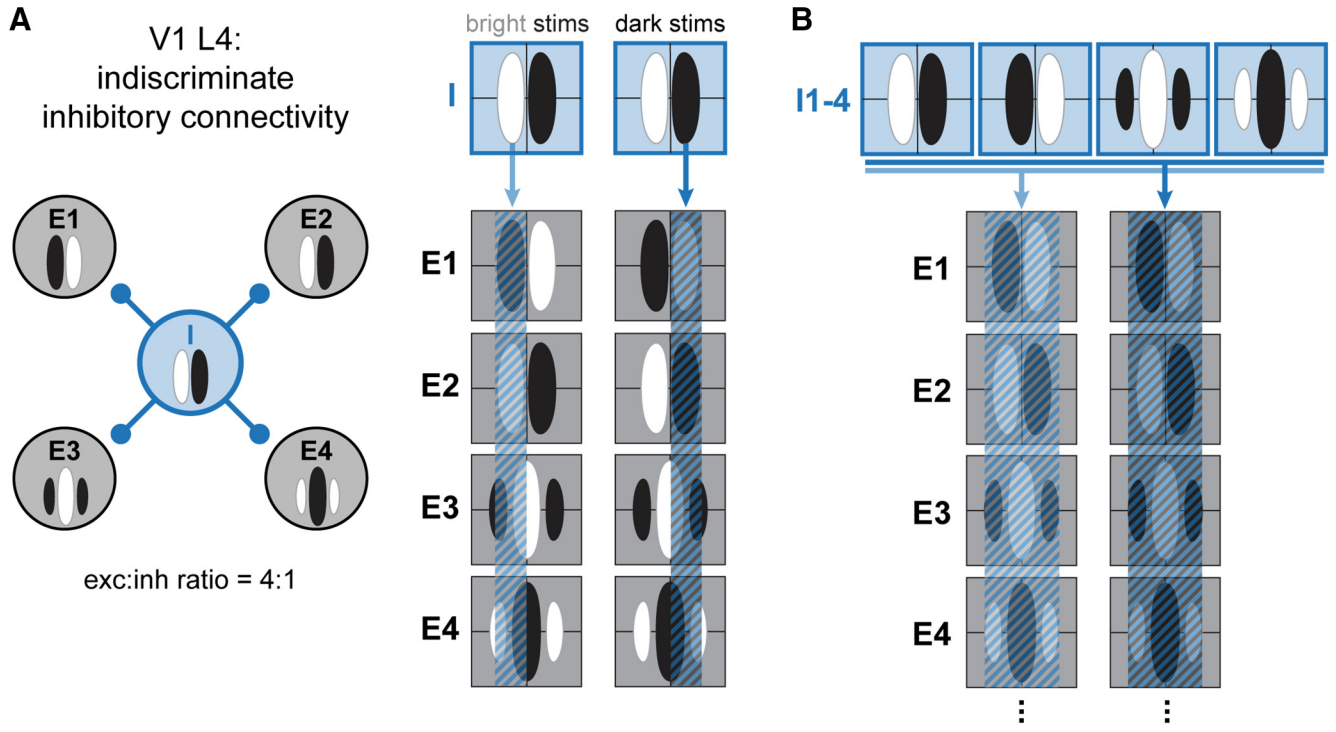

Figure 9. Schematic of indiscriminate inhibitory connectivity. ***A***, Left, Wiring diagram of a single inhibitory cell (I; blue) synaptically connected to four excitatory cells (E1–E4, black). Anatomy suggests that inhibitory cells in V1 L4 are indiscriminately connected to cells within 150 μm of their cell bodies. Right, 2D RFs of all 5 cells, overlaid with the footprint of inhibition imposed by the inhibitory cell in response to bright (left) and dark (right) stimuli. The distribution of inhibition from this single inhibitory cell on each excitatory cell has no spatial correlation with the RF of the postsynaptic cell. ***B***, When multiple inhibitory cells with different RFs (I1–I4) project to the same set of excitatory cells, the summed footprints of the inhibitory output cover the RF of each postsynaptic cell, generating broad inhibition.

To determine whether broad inhibition is consistent with the modulation of gE and gI in response to drifting gratings, as observed in previous studies (Anderson et al., 2000; Monier et al., 2008; Tan et al., 2011), we simulated the V_m, gE, and gI of each cell in response to a drifting grating, as in Figure 5. The example cell in Figure 10 showed the modulation of gE (Fig. 10*G*, bottom, red) in cophase with the V_m modulation (Fig. 10*G*, top) and near antiphase with gI (Fig. 10*G*, bottom, blue), despite the broad inhibition across its RF (Fig. 10*D*, right). For this cell, the near-antiphase modulation of gI relative to gE arose from the slightly greater bright-evoked gI toward the OFF subregion and slightly greater dark-evoked gI toward the ON subregion (Fig. 10*D*, right). Following the diversity of spatial gI distributions generated by random connectivity, the simulated population exhibited a diversity of gE–gI phase shifts (Fig. 10*H*).

Slight OFF-anchoring bias of RFs generates OFF subregion-biased inhibition

Recent studies have suggested that the retinotopy of simple cell RFs is anchored by OFF subregions (Kremkow et al., 2016a; Lee et al., 2016b). We incorporated OFF-anchoring by adding a bias of RF position for both excitatory and inhibitory cells (see Materials and Methods). A mere 8% bias toward OFF-anchoring generated gI centers significantly closer to the OFF subregion, although with a smaller magnitude than that observed in the data (8% bias: gI centers median = 0.56 RFU; significantly different from 0.5, $p = 0.037$, $n = 157$, signed rank test). A 20% bias produced only subtle shifts in RF locations (Fig. 11*A*) and maintained broad inhibition (Fig. 11*B*,*C*), but the resulting gI distributions were centered significantly closer to the OFF subregion (Fig. 11*D*, 20% bias: gI centers median = 0.62 RFU; significantly different from 0.5, $p = 0.0032$, $n = 157$, signed rank test), reproducing the bias observed in the data (Fig. 4). This population also exhibited a diversity of gE–gI phase shifts (Fig. 11*E*).

Discussion

Our results contribute three major findings to our understanding of sensory processing in V1. First, visually evoked depolarizing synaptic responses in simple cells are generated by a mix of excitation and inhibition due to a broad footprint of inhibition across their RFs. Second, this RF-wide inhibition is usually larger toward the OFF subregions. Finally, we show that broad inhibition generates a diversity of phase shifts between excitation and inhibition in response to drifting gratings, including antiphase relationships. These findings have implications for both the anatomical connectivity of L4 and the functional processing of visual stimuli by the circuit.

Simple cell RFs and the push–pull model

Previous work suggested spatially restricted gE and gI based on their temporal antiphase in response to optimally oriented drifting gratings, and spatial and temporal antiphase in response to dense 1D noise (Ferster, 1988; Hirsch et al., 1998; Anderson et al., 2000; Monier et al., 2003, 2008; Priebe and Ferster, 2005). Our finding of broad inhibition across simple cell RFs challenges the assumptions of spatially restricted inhibitory connectivity arising from these results, but it is compatible with the results themselves. Our simple simulations of gE and gI responses to drifting gratings produce a more diverse set of gE–gI phase shifts than is traditionally expected. One possible explanation is that temporal dynamics, including delays, might contribute to a more consistently antiphase relationship between gE and gI. These dynamics are

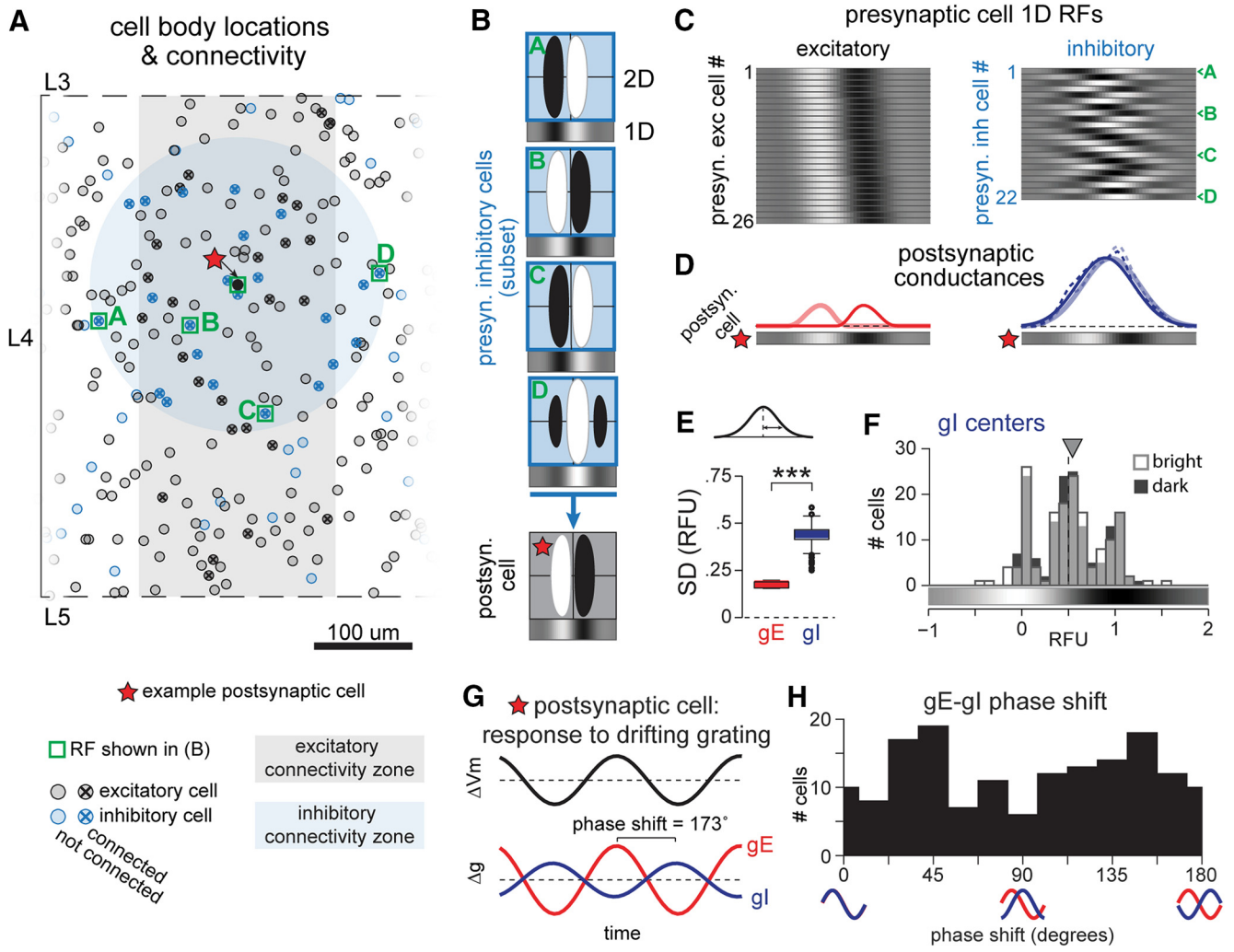

Figure 10. Indiscriminate inhibitory connectivity generates broad inhibition and temporally off-phase modulated gE and gI to drifting gratings. ***A***, Plot of cell body locations of simulated neurons in a section of cortex. Black circles represent excitatory neurons; blue, inhibitory neurons. Red star indicates the example postsynaptic cell used in this figure. Circles with an "X" inside are functionally connected (presynaptic) to the postsynaptic cell. Light black and blue regions denote the areas from which excitatory and inhibitory presynaptic cells were drawn. Only excitatory neurons whose RFs correlate >0.5 with the postsynaptic cell were considered functionally connected. Layer 4 borders indicated by dashed lines. Green boxes and letters indicate cells whose RFs are shown in ***B*** and are indicated in ***C***. ***B***, 2D and 1D RFs of the 5 boxed cells in ***A***. RFs represent bright − dark V_m responses. RFs are displaced for clarity but in fact overlap when aligned to background grids. The RFs shift along the azimuth by a factor of 0.5 RF widths/1 mm of horizontal cortex. ***C***, 1D RFs of the excitatory (left) and inhibitory (right) cells presynaptic to the example cell. RFs are ordered by horizontal location in cortex, which correlates with RF location in visual space. ***D***, Summed presynaptic responses of excitatory (red, left) and inhibitory (blue, right) cells to bright and dark stimuli. Dashed lines are raw values, solid lines are Gaussian fits. 1D RF of the postsynaptic cell is shown below each plot. ***E***, SDs of Gaussian fits of gE and gI for $n = 157$ cells. ***F***, Distribution of gI centers in response to bright (light gray) or dark (black) stimuli. ***G***, Simulated response of the example cell to a drifting grating stimulus, computed as in Figure 5. ***H***, Distribution of gE– gI phase shifts from $n = 157$ cells. ***$p < 0.001$.

likely even more complex for drifting gratings than for flashed bars, as the former stimuli involve constant integration of spatiotemporally variable contrasts across the span of and beyond the RF and therefore engage interactions between many local cortical neurons and other brain areas. Our results derive from flashed stimuli, which selectively and briefly activate constrained parts of the visual pathway and are therefore more appropriate for understanding functional inhibitory connectivity. By limiting our analysis to the first ~50 ms of the synaptic response, we focused on conductances that reflect minimal recurrent and feedback processing, which likely play a large role in determining the temporal dynamics of responses to ongoing stimuli. A more comprehensive model, beyond the scope of this study, will be necessary to confirm the role of local processing in ongoing stimuli.

Furthermore, however, the available data from the literature do not suggest a consistent antiphase modulation of gE and gI in response to gratings, but rather a diverse mix of phase shifts. There are examples of near-cophase gE and gI to drifting gratings in Anderson et al. (2000) and Tan et al. (2011) and to optimally oriented moving bars in Monier et al. (2008). These examples are consistent with the diversity of gE and gI modulation in response to drifting gratings arising from the diversity of broad gI distributions in our data and models. Furthermore, cophase modulation of gE and gI, observed in mouse visual cortex (Tan et al., 2011), is also consistent with spatially broad inhibition.

Our finding that excitatory stimuli limited to a single RF subregion concomitantly drive excitation and inhibition is in agreement with previous studies in cat L4 simple cells (Borg-Graham et al., 1998; Frégnac et al., 2003; Monier et al., 2008), although they did not report the position of the stimuli with respect to the RF. We show that excitatory stimuli that do not impinge on neighboring subregions evoke both excitation and inhibition.

Furthermore, our results agree with studies of thalamorecipient neurons in other sensory systems (Wehr and Zador, 2003; Tan et al., 2004; Wilent and Contreras, 2005; Higley and Contreras, 2006; Isaacson and Scanziani, 2011; Frégnac and Bathellier, 2015; Kremkow et al., 2016a) and with recent findings in mouse V1 simple cells (Liu et al., 2010; Haider et al., 2013; Li et al., 2015). The latter findings were attributed to species differences between the mouse and cat, but our data instead suggest that broad inhibition is a common feature of mammalian simple cell RFs. Some species differences do exist: in cat, inhibitory cells are well tuned for orientation, whereas in mouse, this tuning is much more broad in the orientation domain, and inhibitory cells do not generally have simple RFs (Niell and Stryker, 2008). Therefore while broad inhibition may be a common feature of simple cell RFs, the source of this inhibition is likely different between species.

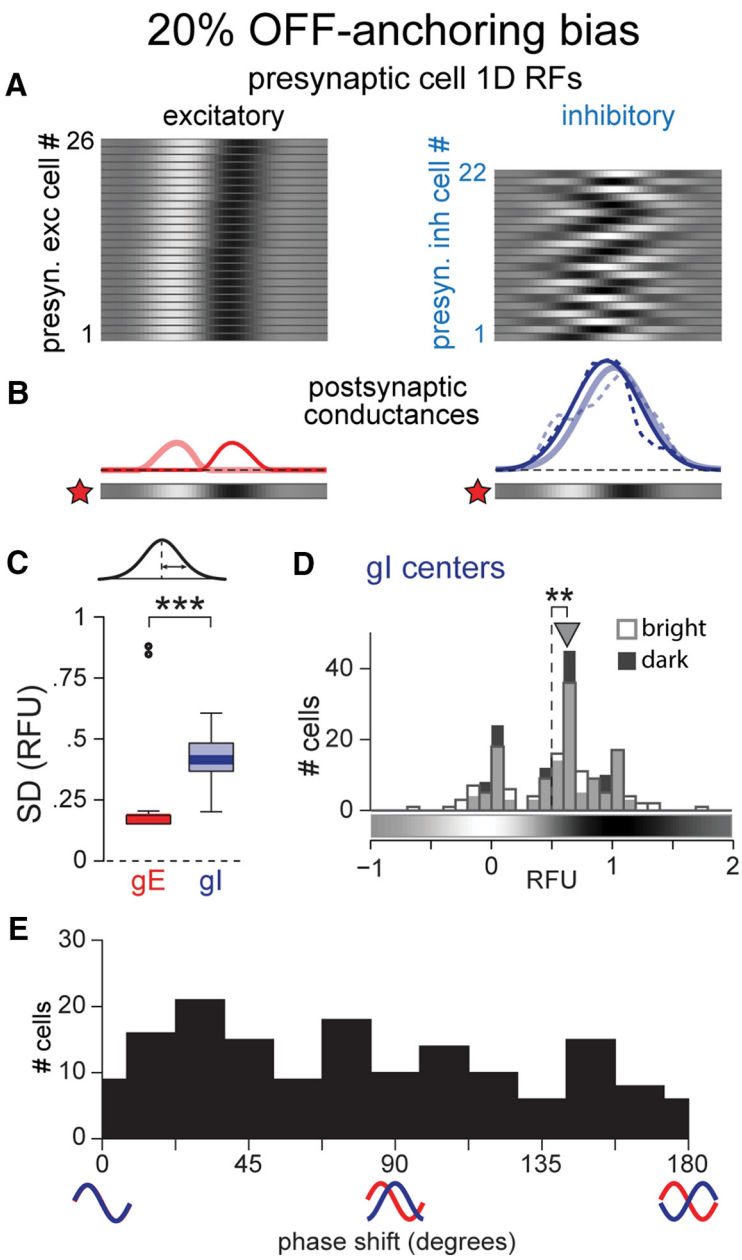

Figure 11. OFF-anchored RF positions generate OFF subregion-biased inhibition. ***A–E***, As in Figure 10, *C–F*, and *H*, but with 20% OFF-anchoring bias. $^{**}p < 0.01$; $^{***}p < 0.001$.

Functional connectivity

Spatially restricted excitation was predicted by Hubel and Wiesel (1962) to arise from the precise connections between LGN thalamocortical cells and L4 simple cells in V1. Such specificity was supported by cross-correlation extracellular studies (Reid and Alonso, 1995; Alonso et al., 2001) and was more recently confirmed by intracellular recordings from L4 simple cells showing connections from LGN neurons only for cell pairs with overlapping RFs (Sedigh-Sarvestani et al., 2017). Our results lend further support to a spatially restricted scheme for excitation, originating from the alignment (Hubel and Wiesel, 1962; Reid and Alonso, 1995) and synchrony (Usrey et al., 2000; Stanley et al., 2012) of LGN inputs, and amplified by local excitation from similarly tuned neurons (Smith and Kohn, 2008; Denman and Contreras, 2014; Cossell et al., 2015).

For inhibition, however, our results suggest a simpler scheme for the wiring in the L4 circuit, rather than spatially restricted inhibitory connections (Troyer et al., 1998; Anderson et al., 2000; Miller et al., 2001; Alitto and Dan, 2010; Frégnac and Bathellier, 2015). We hypothesize that indiscriminate connections from inhibitory neurons to their nearby neighbors (Kisvárday et al., 1985; Fino and Yuste, 2011; Packer and Yuste, 2011) generate a spatial footprint of inhibition reflecting the RFs of inhibitory cells, unrelated to the relative position, size, or phase of the RFs of postsynaptic targets. The spatial distribution of visually driven inhibition in a simple cell therefore represents the joint spatial spread of the RFs of their inhibitory presynaptic neurons. From this broad inhibition, excitatory subregions emerge by the relative dominance of spatially confined excitatory drive, which is discussed above.

An alternative but not mutually exclusive hypothesis for the generation of broad inhibition is that L4 interneurons are complex cells and therefore respond to both bright and dark stimuli across their RF (Lauritzen and Miller, 2003). This is consistent with the RF-wide gI shown here. While complex cells with smooth dendrites and FS characteristics have been found in the middle layers of cat V1 (Hirsch et al., 2003; Cardin et al., 2007), the majority of smooth/FS cells in both studies were simple cells.

Delayed inhibition

In other sensory modalities and in mouse V1, the onset of inhibition accompanying excitation was delayed by a few milliseconds (Wehr and Zador, 2003; Tan et al., 2004; Wilent and Contreras, 2005; Higley and Contreras, 2006; Liu et al., 2010, 2011; Li et al., 2015). The delay in our study (~5 ms) was longer than in the other sensory systems (~1–2 ms) and was consistent with the mouse studies (but see Liu et al., 2011). We suggest that delayed inhibition is built into the architecture of L4 circuits engaged by thalamic

input (Gibson et al., 1999; Cruikshank et al., 2007, 2010). In the rapidly responding auditory and somatosensory systems, with cortical spike latencies of <10 ms and sparse output of only a few spikes per stimulus, delayed inhibition contributes to spike precision (Wehr and Zador, 2003; Higley and Contreras, 2006) or stimulus selectivity (Wilent and Contreras, 2005).

In the visual system, responses to flashed stimuli have longer cortical latencies and prolonged spike responses (Fig. 6*A*, >30 ms), suggesting that the short delay between excitation and inhibition may not be functionally relevant. However, in natural vision, neuronal responses are faster and more precise (Butts et al., 2007, Baudot et al., 2013). Our findings showing strong inhibition driven by excitatory stimuli lend additional support to the hypothesis that a tight temporal coupling between excitation and inhibition allows for precise and sparse spiking in visual cortex during natural scenes (Baudot et al., 2013, Kremkow et al., 2016b). A modeling study (Liu et al., 2011) further demonstrated that shorter delays between excitation and inhibition produced stronger effects of inhibition on dynamic range and orientation tuning in simple cells.

OFF subregion-biased inhibition

A surprising result from this study is that the broad inhibition is generally strongest toward the OFF subregion. This spatial asymmetry leads to more efficient suppression of simple cell output by bright stimuli than by dark stimuli. These data conform well with recent studies showing that LGN afferents and simple cell retinotopy are anchored by OFF subregions (Jin et al., 2011; Kremkow et al., 2016a; Lee et al., 2016a). While these studies did not distinguish excitatory from inhibitory neurons, we expect that future studies will confirm our prediction that inhibitory neurons also exhibit OFF subregion anchoring. Our phenomenological implementation of an OFF bias in the arrangement of RF phases yielded an OFF-biased distribution of inhibition in simple cell RFs. While the developmental and anatomical mechanisms of RF OFF anchoring is not yet known, Kremkow et al. (2016a) further hypothesized that it may arise from earlier development of the OFF pathway (Albus and Wolf, 1984), and we hypothesize that such a developmental rule may similarly generate OFF-biased inhibition.

References

Ahmed B, Anderson JC, Douglas RJ, Martin KA, Nelson JC (1994) Polyneuronal innervation of spiny stellate neurons in cat visual cortex. J Comp Neurol 341:39–49. CrossRef Medline

Ahmed B, Anderson JC, Martin KA, Nelson JC (1997) Map of the synapses onto layer 4 basket cells of the primary visual cortex of the cat. J Comp Neurol 380:230–242. CrossRef Medline

Albus K, Wolf W (1984) Early post-natal development of neuronal function in the kitten's visual cortex: a laminar analysis. J Physiol 348:153–185. CrossRef Medline

Alitto HJ, Dan Y (2010) Function of inhibition in visual cortical processing. Curr Opin Neurobiol 20:340–346. CrossRef Medline

Allison JD, Kabara JF, Snider RK, Casagrande VA, Bonds AB (1996) GABAB-receptor-mediated inhibition reduces the orientation selectivity of the sustained response of striate cortical neurons in cats. Vis Neurosci 13:559–566. CrossRef Medline

Alonso JM, Usrey WM, Reid RC (2001) Rules of connectivity between geniculate cells and simple cells in cat primary visual cortex. J Neurosci 21:4002–4015. Medline

Anderson JS, Carandini M, Ferster D (2000) Orientation tuning of input conductance, excitation, and inhibition in cat primary visual cortex. J Neurophysiol 84:909–926. Medline

Azzopardi G, Rodríguez-Sánchez A, Piater J, Petkov N (2014) A push-pull CORF model of a simple cell with antiphase inhibition improves SNR and contour detection. PLoS One 9:e98424. CrossRef Medline

Baudot P, Levy M, Marre O, Monier C, Pananceau M, Frégnac Y (2013) Animation of natural scene by virtual eye-movements evokes high precision and low noise in V1 neurons. Front Neural Circuits 7:206. CrossRef Medline

Beaulieu C, Colonnier M (1983) The number of neurons in the different laminae of the binocular and monocular regions of area 17 in the cat. J Comp Neurol 217:337–344. CrossRef Medline

Binzegger T, Douglas RJ, Martin KA (2004) A quantitative map of the circuit of cat primary visual cortex. J Neurosci 24:8441–8453. CrossRef Medline

Bonhoeffer T, Kim DS, Malonek D, Shoham D, Grinvald A (1995) Optical imaging of the layout of functional domains in area 17 and across the area 17/18 border in cat visual cortex. Eur J Neurosci 7:1973–1988. CrossRef Medline

Borg-Graham LJ, Monier C, Frégnac Y (1998) Visual input evokes transient and strong shunting inhibition in visual cortical neurons. Nature 393:369–373. CrossRef Medline

Butts DA, Weng C, Jin J, Yeh CI, Lesica NA, Alonso JM, Stanley GB (2007) Temporal precision in the neural code and the timescales of natural vision. Nature 449:92–95. CrossRef Medline

Cardin JA, Palmer LA, Contreras D (2007) Stimulus feature selectivity in excitatory and inhibitory neurons in primary visual cortex. J Neurosci 27:10333–10344. CrossRef Medline

Cardin JA, Kumbhani RD, Contreras D, Palmer LA (2010) Cellular mechanisms of temporal sensitivity in visual cortex neurons. J Neurosci 30:3652–3662. CrossRef Medline

Connors BW, Prince DA (1982) Effects of local anesthetic QX-314 on the membrane properties of hippocampal pyramidal neurons. J Pharmacol Exp Ther 220:476–481. Medline

Contreras D, Palmer L (2003) Response to contrast of electrophysiologically defined cell classes in primary visual cortex. J Neurosci 23:6936–6945. Medline

Cossell L, Iacaruso MF, Muir DR, Houlton R, Sader EN, Ko H, Hofer SB, Mrsic-Flogel TD (2015) Functional organization of excitatory synaptic strength in primary visual cortex. Nature 518:399–403. CrossRef Medline

Cruikshank SJ, Lewis TJ, Connors BW (2007) Synaptic basis for intense thalamocortical activation of feedforward inhibitory cells in neocortex. Nat Neurosci 10:462–468. CrossRef Medline

Cruikshank SJ, Urabe H, Nurmikko AV, Connors BW (2010) Pathway-specific feedforward circuits between thalamus and neocortex revealed by selective optical stimulation of axons. Neuron 65:230–245. CrossRef Medline

Denman DJ, Contreras D (2014) The structure of pairwise correlation in mouse primary visual cortex reveals functional organization in the absence of an orientation map. Cereb Cortex 24:2707–2720. CrossRef Medline

Ferster D (1986) Orientation selectivity of synaptic potentials in neurons of cat primary visual cortex. J Neurosci 6:1284–1301. Medline

Ferster D (1988) Spatially opponent excitation and inhibition in simple cells of the cat visual cortex. J Neurosci 8:1172–1180. Medline

Ferster D, Miller KD (2000) Neural mechanisms of orientation selectivity in the visual cortex. Annu Rev Neurosci 23:441–471. CrossRef Medline

Fino E, Yuste R (2011) Dense inhibitory connectivity in neocortex. Neuron 69:1188–1203. CrossRef Medline

Frégnac Y, Bathellier B (2015) Cortical correlates of low-level perception: from neural circuits to percepts. Neuron 88:110–126. CrossRef Medline

Frégnac Y, Monier C, Chavane F, Baudot P, Graham L (2003) Shunting inhibition, a silent step in visual cortical computation. J Physiol Paris 97:441–451. CrossRef Medline

Gabbott PL, Somogyi P (1986) Quantitative distribution of GABA-immunoreactive neurons in the visual cortex (area 17) of the cat. Exp Brain Res 61:323–331. Medline

Gibson JR, Beierlein M, Connors BW (1999) Two networks of electrically coupled inhibitory neurons in neocortex. Nature 402:75–79. CrossRef Medline

Haider B, Duque A, Hasenstaub AR, McCormick DA (2006) Neocortical network activity in vivo is generated through a dynamic balance of excitation and inhibition. J Neurosci 26:4535–4545. CrossRef Medline

Haider B, Häusser M, Carandini M (2013) Inhibition dominates sensory responses in the awake cortex. Nature 493:97–100. CrossRef Medline

Heiss JE, Katz Y, Ganmor E, Lampl I (2008) Shift in the balance between excitation and inhibition during sensory adaptation of S1 neurons. J Neurosci 28:13320–13330. CrossRef Medline

Higley MJ, Contreras D (2006) Balanced excitation and inhibition deter-

mine spike timing during frequency adaptation. J Neurosci 26:448–457. CrossRef Medline
Hirsch JA (2003) Synaptic physiology and receptive field structure in the early visual pathway of the cat. Cereb Cortex 13:63–69. CrossRef Medline
Hirsch JA, Alonso JM, Reid RC, Martinez LM (1998) Synaptic integration in striate cortical simple cells. J Neurosci 18:9517–9528. Medline
Hirsch JA, Martinez LM, Pillai C, Alonso JM, Wang Q, Sommer FT (2003) Functionally distinct inhibitory neurons at the first stage of visual cortical processing. Nat Neurosci 6:1300–1308. CrossRef Medline
Hubel DH, Wiesel TN (1959) Receptive fields of single neurones in the cat's striate cortex. J Physiol 148:574–591. CrossRef Medline
Hubel DH, Wiesel TN (1962) Receptive fields, binocular interaction and functional architecture in the cat's visual cortex. J Physiol 160:106–154. CrossRef Medline
Isaacson JS, Scanziani M (2011) How inhibition shapes cortical activity. Neuron 72:231–243. CrossRef Medline
Jin J, Wang Y, Swadlow HA, Alonso JM (2011) Population receptive fields of ON and OFF thalamic inputs to an orientation column in visual cortex. Nat Neurosci 14:232–238. CrossRef Medline
Jones JP, Palmer LA (1987a) An evaluation of the two-dimensional Gabor filter model of simple receptive fields in cat striate cortex. J Neurophysiol 58:1233–1258. Medline
Jones JP, Palmer LA (1987b) The two-dimensional spatial structure of simple receptive fields in cat striate cortex. J Neurophysiol 58:1187–1211. Medline
Kisvárday ZF, Martin KA, Whitteridge D, Somogyi P (1985) Synaptic connections of intracellularly filled clutch cells: a type of small basket cell in the visual cortex of the cat. J Comp Neurol 241:111–137. CrossRef Medline
Kremkow J, Jin J, Wang Y, Alonso JM (2016a) Principles underlying sensory map topography in primary visual cortex. Nature 533:52–57. CrossRef Medline
Kremkow J, Perrinet LU, Monier C, Alonso JM, Aertsen A, Frégnac Y, Masson GS (2016b) Push-pull receptive field organization and synaptic depression: mechanisms for reliably encoding naturalistic stimuli in V1. Front Neural Circuits 10:37. CrossRef Medline
Lauritzen TZ, Miller KD (2003) Different roles for simple-cell and complex-cell inhibition in V1. J Neurosci 23:10201–10213. Medline
Lee KS, Huang X, Fitzpatrick D (2016a) Topology of ON and OFF inputs in visual cortex enables an invariant columnar architecture. Nature 533:90–94. CrossRef Medline
Lee WC, Bonin V, Reed M, Graham BJ, Hood G, Glattfelder K, Reid RC (2016b) Anatomy and function of an excitatory network in the visual cortex. Nature 532:370–374. CrossRef Medline
Li YT, Liu BH, Chou XL, Zhang LI, Tao HW (2015) Strengthening of direction selectivity by broadly tuned and spatiotemporally slightly offset inhibition in mouse visual cortex. Cereb Cortex 25:2466–2477. CrossRef Medline
Liu BH, Li P, Sun YJ, Li YT, Zhang LI, Tao HW (2010) Intervening inhibition underlies simple-cell receptive field structure in visual cortex. Nat Neurosci 13:89–96. CrossRef Medline
Liu BH, Li YT, Ma WP, Pan CJ, Zhang LI, Tao HW (2011) Broad inhibition sharpens orientation selectivity by expanding input dynamic range in mouse simple cells. Neuron 71:542–554. CrossRef Medline
Michalski A, Gerstein GL, Czarkowska J, Tarnecki R (1983) Interactions between cat striate cortex neurons. Exp Brain Res 51:97–107. Medline
Miller KD, Pinto DJ, Simons DJ (2001) Processing in layer 4 of the neocortical circuit: new insights from visual and somatosensory cortex. Curr Opin Neurobiol 11:488–497. CrossRef Medline
Monier C, Chavane F, Baudot P, Graham LJ, Frégnac Y (2003) Orientation and direction selectivity of synaptic inputs in visual cortical neurons: a diversity of combinations produces spike tuning. Neuron 37:663–680. CrossRef Medline
Monier C, Fournier J, Frégnac Y (2008) In vitro and in vivo measures of evoked excitatory and inhibitory conductance dynamics in sensory cortices. J Neurosci Methods 169:323–365. CrossRef Medline
Mulle C, Steriade M, Deschênes M (1985) The effects of QX314 on thalamic neurons. Brain Res 333:350–354. CrossRef Medline
Niell CM, Stryker MP (2008) Highly selective receptive fields in mouse visual cortex. J Neurosci 28:7520–7536. CrossRef Medline
Packer AM, Yuste R (2011) Dense, unspecific connectivity of neocortical parvalbumin-positive interneurons: a canonical microcircuit for inhibition? J Neurosci 31:13260–13271. CrossRef Medline
Palmer LA, Davis TL (1981) Receptive-field structure in cat striate cortex. J Neurophysiol 46:260–276. Medline
Poo C, Isaacson JS (2009) Odor representations in olfactory cortex: "sparse" coding, global inhibition, and oscillations. Neuron 62:850–861. CrossRef Medline
Priebe NJ, Ferster D (2005) Direction selectivity of excitation and inhibition in simple cells of the cat primary visual cortex. Neuron 45:133–145. CrossRef Medline
Ramón y Cajal S (1909) Histologie du système nerveux de l'homme and des vertébrés. Paris, France: Maloine.
Reid RC, Alonso JM (1995) Specificity of monosynaptic connections from thalamus to visual cortex. Nature 378:281–284. CrossRef Medline
Rudolph M, Pospischil M, Timofeev I, Destexhe A (2007) Inhibition determines membrane potential dynamics and controls action potential generation in awake and sleeping cat cortex. J Neurosci 27:5280–5290. CrossRef Medline
Sedigh-Sarvestani M, Vigeland L, Fernandez-Lamo I, Taylor MM, Palmer LA, Contreras D (2017) Intracellular, in vivo, dynamics of thalamocortical synapses in visual cortex. J Neurosci 37:5250–5262. CrossRef Medline
Smith MA, Kohn A (2008) Spatial and temporal scales of neuronal correlation in primary visual cortex. J Neurosci 28:12591–12603. CrossRef Medline
Somogyi P, Soltész I (1986) Immunogold demonstration of GABA in synaptic terminals of intracellularly recorded, horseradish peroxidase-filled basket cells and clutch cells in the cat's visual cortex. Neuroscience 19:1051–1065. CrossRef Medline
Stanley GB, Jin J, Wang Y, Desbordes G, Wang Q, Black MJ, Alonso JM (2012) Visual orientation and directional selectivity through thalamic synchrony. J Neurosci 32:9073–9088. CrossRef Medline
Tan AYY, Brown BD, Scholl B, Mohanty D, Priebe NJ (2011) Orientation selectivity of synaptic input to neurons in mouse and cat primary visual cortex. J Neurosci 31:12339–12350. CrossRef
Tan AY, Zhang LI, Merzenich MM, Schreiner CE (2004) Tone-evoked excitatory and inhibitory synaptic conductances of primary auditory cortex neurons. J Neurophysiol 92:630–643. CrossRef Medline
Tarczy-Hornoch K, Martin KA, Stratford KJ, Jack JJ (1999) Intracortical excitation of spiny neurons in layer 4 of cat striate cortex in vitro. Cereb Cortex 9:833–843. CrossRef Medline
Troyer TW, Krukowski AE, Priebe NJ, Miller KD (1998) Contrast-invariant orientation tuning in cat visual cortex: thalamocortical input tuning and correlation-based intracortical connectivity. J Neurosci 18:5908–5927. Medline
Usrey WM, Alonso JM, Reid RC (2000) Synaptic interactions between thalamic inputs to simple cells in cat visual cortex. J Neurosci 20:5461–5467. Medline
Vigeland LE, Contreras D, Palmer LA (2013) Synaptic mechanisms of temporal diversity in the lateral geniculate nucleus of the thalamus. J Neurosci 33:1887–1896. CrossRef Medline
Wang Y, Jin J, Kremkow J, Lashgari R, Komban SJ, Alonso JM (2015) Columnar organization of spatial phase in visual cortex. Nat Neurosci 18:97–103. CrossRef Medline
Wehr M, Zador AM (2003) Balanced inhibition underlies tuning and sharpens spike timing in auditory cortex. Nature 426:442–446. CrossRef Medline
Wilent WB, Contreras D (2005) Dynamics of excitation and inhibition underlying stimulus selectivity in rat somatosensory cortex. Nat Neurosci 8:1364–1370. CrossRef Medline